SPECIAL DIMES COLLECTION

Relative Dispersion in the Antarctic Circumpolar Current

DHRUV BALWADA,[a] JOSEPH H. LACASCE,[b] KEVIN G. SPEER,[c] AND RAFFAELE FERRARI[d]

[a] *School of Oceanography, University of Washington, Seattle, Washington*
[b] *Department of Geosciences, University of Oslo, Oslo, Norway*
[c] *Geophysical Fluid Dynamics Institute, Florida State University, Tallahassee, Florida*
[d] *Department of Earth, Atmosphere and Planetary Sciences, Massachusetts Institute of Technology, Cambridge, Massachusetts*

(Manuscript received 7 October 2019, in final form 25 November 2020)

ABSTRACT: Stirring in the subsurface Southern Ocean is examined using RAFOS float trajectories, collected during the Diapycnal and Isopycnal Mixing Experiment in the Southern Ocean (DIMES), along with particle trajectories from a regional eddy permitting model. A central question is the extent to which the stirring is local, by eddies comparable in size to the pair separation, or nonlocal, by eddies at larger scales. To test this, we examine metrics based on averaging in time and in space. The model particles exhibit nonlocal dispersion, as expected for a limited resolution numerical model that does not resolve flows at scales smaller than ~10 days or ~20–30 km. The different metrics are less consistent for the RAFOS floats; relative dispersion, kurtosis, and relative diffusivity suggest nonlocal dispersion as they are consistent with the model within error, while finite-size Lyapunov exponents (FSLE) suggests local dispersion. This occurs for two reasons: (i) limited sampling of the inertial length scales and a relatively small number of pairs hinder statistical robustness in time-based metrics, and (ii) some space-based metrics (FSLE, second-order structure functions), which do not average over wave motions and are reflective of the kinetic energy distribution, are probably unsuitable to infer dispersion characteristics if the flow field includes energetic wave motions that do not disperse particles. The relative diffusivity, which is also a space-based metric, allows averaging over waves to infer the dispersion characteristics. Hence, given the error characteristics of the metrics and data used here, the stirring in the DIMES region is likely to be nonlocal at scales of 5–100 km.

KEYWORDS: Diffusion; Dispersion; Internal waves; Lagrangian circulation/transport; Mesoscale processes; Isopycnal mixing

1. Introduction

Oceanic flows are turbulent over a large range of length scales and are very efficient at stirring tracers along isopycnals, enhancing the effects of molecular diffusion by many orders of magnitude (Garrett 2006). The parameterization of this lateral stirring is key to the proper representation of the oceanic transport of heat, carbon, nutrients, and other climatically important tracers in climate models (e.g., Gnanadesikan et al. 2015; Fox-Kemper et al. 2013). The details of these parameterizations are particularly important in the Southern Ocean, where the surface is connected to the deep ocean via sloping isopycnals and along-isopycnal stirring plays a key role in biological production (Uchida et al. 2019, 2020) and ventilation of the deep ocean (Marshall and Speer 2012; Abernathey and Ferreira 2015; Balwada et al. 2018; Jones and Abernathey 2019). To ensure the fidelity of these parameterizations, it is essential that quantitative estimates of stirring are obtained using in situ measurements.

The nature and strength of the lateral or along-isopycnal eddy stirring in the ocean depends on the length scales under consideration. At length scales greater than the size of dominant mesoscale eddies the stirring can approximately be expressed as enhanced molecular diffusion with a constant eddy diffusivity that is $O(1000)\,\mathrm{m^2\,s^{-1}}$ (Zhurbas and Oh 2003; Koszalka et al. 2011; LaCasce et al. 2014; Balwada et al. 2016b; Roach et al. 2016, 2018). On the other hand, at scales smaller than the typical mesoscale eddies, this eddy diffusivity generally increases with the length scale (Richardson 1926; Okubo 1971). At these scales two qualitatively different regimes are possible, which can be categorized based on how stirring influences the rate of Lagrangian particle pair spreading or relative dispersion—nonlocal and local dispersion (Bennett 1984). Nonlocal dispersion occurs when the kinetic energy spectrum is steeper than k^{-3}; in this case stirring is dominated by the largest eddies. Under local dispersion, in contrast, stirring is dominated by eddies comparable in scale to the size of the cluster or tracer patch. Knowledge about which regime is active in the ocean can help to define parameterizations of stirring for use in eddy-permitting models (Cushman-Roisin 2008; Kämpf and Cox 2016).

Observational characterization of the stirring regime is practically difficult, and requires dense sampling with pairs of Lagrangian instruments, which is why most previous studies have focused on the surface ocean using surface drifters (LaCasce and Ohlmann 2003; Koszalka et al. 2009; Lumpkin and Elipot 2010; Poje et al. 2014; van Sebille et al. 2015; Sansón

Denotes content that is immediately available upon publication as open access.

Corresponding author: Dhruv Balwada, dbalwada@uw.edu

DOI: 10.1175/JPO-D-19-0243.1

2015; Beron-Vera and LaCasce 2016; Corrado et al. 2017; Essink et al. 2019). These studies have indicated that a single universal stirring regime is not present everywhere in the surface ocean; some regions show nonlocal dispersion up to roughly the deformation scale and others show local dispersion over the same scale range. Sometimes different metrics also lead to contrasting results in the same region. The large-scale dispersion varies as well, with some suggesting a transition to diffusive spreading (dispersion grows linearly in time) (e.g., Koszalka et al. 2009) and other studies suggesting superdiffusive motion (dispersion grows faster than linear in time) most likely due to advection by the large-scale shear (e.g., LaCasce and Ohlmann 2003).

Deep ocean studies of stirring, which are very rare, rely on sampling the flow using either an anthropogenic tracer (e.g., SF_6) (Ledwell et al. 1998; Watson et al. 2013) or RAFOS floats (Rossby et al. 1986). While a tracer is an excellent means for measuring diapycnal diffusivities (Ledwell et al. 2000; Watson et al. 2013; Ledwell et al. 2016), sampling the details of the lateral spatiotemporal evolution of the tracer by ships is not usually possible and thus limits its usefulness for diagnosing the scale dependence of lateral stirring. RAFOS floats (Swift and Riser 1994), which drift at depth and are acoustically tracked, can be used to characterize and quantify the properties of stirring by evaluating how rapidly float pairs disperse. We are aware of only two previous studies that reported on relative dispersion in the deep ocean (LaCasce and Bower 2000; Ollitrault et al. 2005), both in the North Atlantic Ocean at depths of about 1 km. LaCasce and Bower (2000) concluded the dispersion in the western Atlantic was either local or driven by mean flow shear up to scales of approximately 100km, while the particle pairs separated diffusively in the eastern Atlantic. Ollitrault et al. (2005) also reported local stirring between 40 and 300 km, and some indications of nonlocal stirring at shorter scales.

In this study, we examine stirring at length scales of 5–100 km and depths of 500–2000 m in the southeast Pacific Ocean sector of the Antarctic Circumpolar Current (ACC), using RAFOS floats deployed during the Diapycnal and Isopycnal Mixing Experiment in the Southern Ocean (DIMES) (Balwada et al. 2016b). The floats were deployed in pairs and triplets to resolve smaller-scale dispersion. This work builds on the studies by Tulloch et al. (2014), LaCasce et al. (2014), and Balwada et al. (2016b), which had reported on the eddy diffusivity in the DIMES experiment using both tracer and float observations at scales larger than the dominant mesoscale eddies.

To quantify the flow variability and stirring in the DIMES region we use several different metrics. We start by quantifying the flow variability at different scales using Lagrangian frequency spectra and second-order structure functions in section 3. Stirring or particle dispersion is a result of the integrated effect of the flow variability, and is usually quantified and categorized as local versus nonlocal using metrics that either quantify temporal evolution or spatial structure (Table 1). The pair separation probability distribution function (PDF), and its moments, e.g., the relative dispersion and kurtosis, fall under the time-based metrics. These quantify the temporal evolution of the separation between pairs of particles and are discussed in section 4. The relative diffusivity, discussed in section 5, quantifies the rate of change of relative dispersion. As the averages are conditioned by separation, the relative diffusivity is a space-based metric. Finite-size Lyapunov exponents (FSLE), discussed in section 6, quantify the rate at which particle pairs at different scales separate and is also a space-based metric. Space-based metrics advantageously employ more and more pairs at larger separations, since the same pairs usually visit the larger scales more often than the smaller scales. In contrast, the time-based metrics are limited at all time by the number of samples at the initial pair separation. A summary of the different metrics is presented in Table 1, and Table 2 provides a quick overview of the results.

2. Data and methods

a. *Lagrangian trajectories*

We examine two sets of Lagrangian trajectories: RAFOS floats released during the DIMES experiment (Balwada et al. 2016b), and numerical particles advected in a MITgcm simulation of the southeast Pacific Ocean and Scotia Sea (LaCasce et al. 2014).

The DIMES RAFOS floats, referred to as the floats in the rest of the manuscript, were released in 2009 and 2010 along the 105°W meridian and between 54° and 60°S, spanning the ACC at this F1 location (Figs. 1a,c). Acoustic tracking was used to determine their position once per day. The motion of the floats was primarily along isobars, and they were spread over a depth range of 500–2000 m, with the greatest sampling near depths of 750 and 1400 m (Fig. 1d). In this study we grouped the floats into two depth bins: shallow (500–1000 m) and deep (1000–1800 m), and only considered segments of the trajectories to the west of 80°W. The data to the east of 80°W, in the Scotia Sea, are not considered because the floats there rarely came within 100 km of each other.

The MITgcm numerical particles, referred to as particles in the rest of the manuscript, are the same as those used in LaCasce et al. (2014) (Fig. 1b). The velocity fields used to advect the particles were simulated using the MITgcm with a horizontal resolution of 5 km and 70 vertical levels. The model domain spanned 160°–20°W and 75°–35°S, and was forced at the lateral boundaries by the Ocean Comprehensive Atlas (OCCA; Forget 2010) and at the surface by ECMWF ERA-Interim 6h wind fields (Berrisford et al. 2009). Details of the simulation and comparison to hydrography can be found in Tulloch et al. (2014). One hundred particles were released along 150°W at 20 vertical levels, between 75° and 60°S, at the numerical grid separation of 5 km every 10 days for 120 days—12 releases totaling to 1200 particles. The particles were advected using one-day averaged 3D velocity fields, since the model had negligible variance at faster time scales. Correspondingly, the particle positions were saved at a daily resolution. This provided 1200 particle trajectories at each of the 20 levels from 300 to 3000 m.

The velocity time series following the float and particle trajectories was calculated using discrete forward differences $\{u(t) = [x(t + \delta t) - x(t)]/\delta t\}$, except at the end points where a backward difference was used. As the temporal resolution of the floats (δt) is 1 day, the variability at periods faster than

TABLE 1. Different dispersion regimes, conditions under which they are applicable, corresponding relative diffusivities [Eqs. (3) and (5), section 5, appendix C], PDF solutions to the Fokker–Plank equation [Eq. (4), section 4, appendix B], the corresponding moments (section 4), and the FSLE scalings [Eq. (6), section 6] (Graff et al. 2015; Foussard et al. 2017). The square brackets note the equations and sections where the different metrics are discussed. Here, β is proportional to the third root of the energy flux across scales or the energy dissipation rate, $I_n()$ is the n-order modified Bessel function, $M()$ is the Kummer's function, T_L is proportional to the inverse cubic root of the enstrophy dissipation rate or the inverse square root of the total enstrophy, C_n are constants, and other expressions are the same as defined in the text. The text (asymptotic) implies that the expressions are for the asymptotic limit.

Dispersion regime	Conditions of validity	Relative diffusivity $[\kappa(r,t)]$	Pair separation PDF $[p(r,t\|r_0)]$	Relative dispersion $[r^2(t\|r_0)]$	Kurtosis (r^4/r^2)	FSLE $[\lambda(r)]$
Ballistic	Initial time, memory of initial conditions still present	$t\mathbb{S}2_{ll}(r)$	—	$r_0^2(1+C_1t^2)$	—	—
Nonlocal	Intermediate time, pair velocities are correlated, $E(k) \sim k^{-3}$ or steeper spectrum	r^2/T_L	$\frac{1}{4\pi^{3/2}(t/T_L)^{1/2}r_0^2}\exp\left[-\frac{(\ln r/r_0 + 2t/T)^2}{4t/T_L}\right]$	$r_0^2\exp\left(\frac{8t}{T_L}\right)$	e^{8t/T_L}	r^0
Richardson (local)	Intermediate time, pair velocities are correlated, $E(k) \sim k^{-5/3}$	$\beta r^{4/3}$	$\frac{3}{4\pi\beta t r_0^{2/3} r^{2/3}} I_2\left(\frac{9r_0^{1/3}r^{1/3}}{2\beta t}\right)\exp\left[-\frac{9(r_0^{2/3}+r^{2/3})}{4\beta t}\right]$	$\frac{5!}{2}\left(\frac{4\beta t}{9}\right)^3 M\left(6,3,\frac{9r_0^{2/3}}{4\beta t}\right)\exp\left(-\frac{9r_0^{2/3}}{4\beta t}\right)$, [visually similar to $(r_0^{2/3}+C_2t)^3$] $\sim t^3$ (asymptotic)	5.6 (asymptotic)	$r^{-2/3}$
Diffusive	Long time, pair velocities are uncorrelated	Constant (κ_2)	$\frac{1}{2\pi\kappa_2 t}\exp\left(-\frac{r_0^2+r^2}{4\kappa_2 t}\right) I_0\left(\frac{r_0 r}{2\kappa_2 t}\right)$	$4\kappa_2 t$ (asymptotic)	2 (asymptotic)	r^{-2}

1 day (the inertial period is 14 h in this region) is aliased to longer periods.

b. *Pair selection*

In this study, two different kinds of metrics are considered; time-based metrics averaged at a fixed time and space-based metrics average at fixed spatial scales. The time-based metrics, such as relative dispersion, are a conditional average over pairs with the same initial pair separation ($r_0 \pm \delta$), and this averaging is indicated by $\langle . \rangle_{r_0}$. The space-based metrics, such as structure functions, relative diffusivity, and finite size Lyapunov exponents, average over all pairs that pass through a separation bin, irrespective of the initial pair separation, and this averaging is indicated by $\langle . \rangle$.

Selecting pairs for time-based metrics conditioned on initial separation ($\langle . \rangle_{r_0}$) is trivial in the numerical model because the particles were initialized on a discrete grid. We use particle pairs that were initially released at the same depth and at a particular r_0. When considering the observations, a few choices need to be made due to the following considerations: the floats are not released on a uniform grid, the floats are not all at the same depth due to slight irregularities in instrument ballasting, and there are some gaps in the float time series due to tracking problems.

When analyzing the floats, we use pairs that might be an original pair, a pair released together, or a chance pair, a pair that happens to pass in close proximity ($r_0 \pm \delta r$) due to the flow, and we do not distinguish between the two in the rest of this study (Morel and Larceveque 1974; LaCasce and Bower 2000). We chose r_0 to be relatively large to ensure that a sufficient number of pairs are available; this caused most pairs to be chance pairs as most original pairs were released at smaller initial separation. In some cases a pair time series might return to a separation of r_0 at a later time; we considered this to be the origin of a new chance pair time series if this return happened at least 25 days after the first time the pair members were r_0 apart. However, instances of this were rare and did not contribute significantly to the samples used in this study. We use pair time series with a length of 100 days, since the pair velocities generally decorrelate before that time (shown later). Any pair with less than 25 days of data during this 100-day period is discarded. Finally, to minimize the impact of vertical shear on the separation rates we divided the floats into a shallow set (500–1000 m) and a deep set (1000–1800 m), and only considered pairs with trajectories vertically within 200 m of each other.

Two initial float separation sets, 10–15 km and 30–35 km, were chosen to allow for sufficient sampling. The first baroclinic deformation radius in this region is approximately 15 km (Chelton et al. 1998), hence the smaller initial separation set partially sampled this scale. The shallow sets (500–1000 m) contain approximately 50 and 100 pairs in the two r_0 bins, and the deep sets (1000–1800 m) contain approximately 90 and 180 pairs in the two r_0 bins (Fig. 1e). The number of pairs in each set did not vary substantially over the course of the 100 days considered here. Most pairs evolved at vertical separations of less than 50 m (Fig. 1d). Since most of the strong vertical shear in the interior ocean is associated with high-frequency wave-like motions that do not cause much lateral dispersion, we anticipate the impact of this high-frequency vertical shear on most of the dispersion metrics to be small. Further, the mean

TABLE 2. Summary of metrics over scales at which pair velocities are correlated: spatial scales smaller than 100 km and temporal scales smaller than 50–100 days. The variability metrics are discussed in section 3, and the stirring metrics are discussed in sections 4 (relative dispersion and kurtosis), 5 (relative diffusivity), and 6 (finite-size Lyapunov exponents).

	Domain and averaging	Model particles	RAFOS floats	Summary/comments
Variability metrics				
Lagrangian frequency spectra	Frequency, averaging over all trajectories	$\omega^{-5\sim-4}$	$\omega^{-4\sim-3}$ ($\omega <$ 1/10 days); ($\omega^{-1\sim-1/2}\omega >$ 1/10 days)	Enhanced observed variability, likely due to waves aliased to subinertial frequencies
Second-order structure functions	Space-based, averaging over all sample pairs in bin	r^2	$r^{2/3\sim1}$	Enhanced observed variability, likely due to waves aliased to subinertial frequencies
Stirring metrics				
Relative dispersion	Time-based, averaging conditioned on fixed initial pair separation	Nonlocal	Consistent with model within error bars	Limited numbers of float pairs do not allow an unambiguous categorization, but similarity to particles is suggestive of nonlocal dispersion.
Kurtosis	Time-based, averaging conditioned on fixed initial pair separation	Nonlocal	Consistent with model within error bars	Limited numbers of float pairs do not allow an unambiguous categorization, but similarity to particles is suggestive of nonlocal dispersion.
Relative diffusivity	Space-based, averaging over all sample pairs in bin	r^2; nonlocal	$r^{4/3}$ (Δt = 1 day); $r^{1.5\sim2}$ (Δt = 6 days); consistent with model within error bar at larger Δt	For floats a steepening of relative diffusivity power law with temporal averaging, to match the particle diffusivity, is highly suggestive of nonlocal dispersion
Finite-size Lyapunov exponents	Space-based, averaging over all sample pairs in bin	r^0; nonlocal	$r^{-1\sim-2/3}$; suggests local	Waves, which do not cause any dispersion, can cause FSLE to appear local even when the dispersion is nonlocal

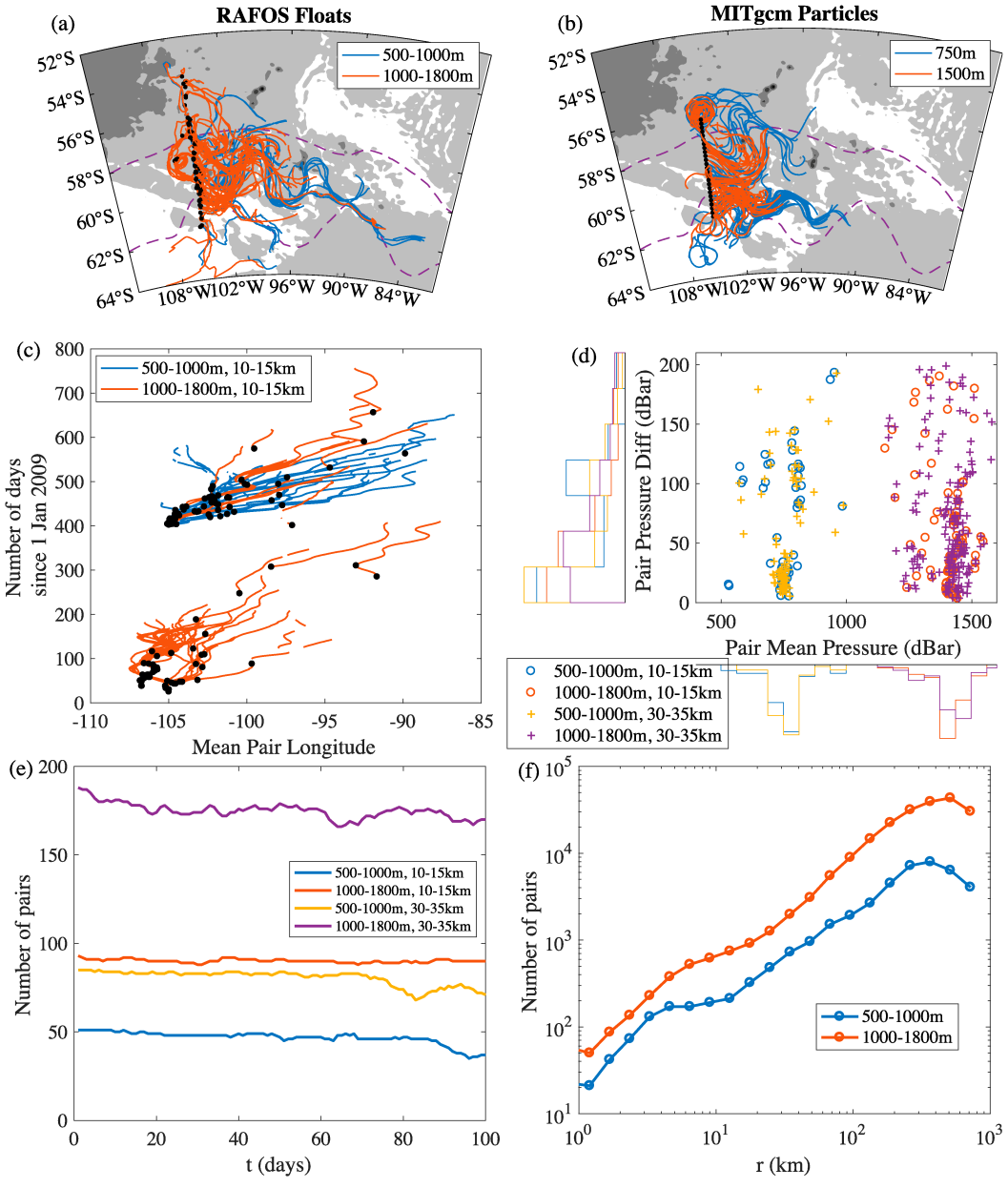

FIG. 1. (a) The 100-day trajectories of RAFOS floats and (b) a representative set of numerical particles from the MITgcm simulation at different depths. The black dots indicate the position of the trajectory on the first day. The climatological Sub-Antarctic Front (SAF) and Polar Front (PF) are marked by dashed purple lines (Orsi et al. 1995). The gray colors represent the bathymetry, with the lightest contour color starting at 6000-m depth, and decreasing by 1000-m intervals as contour regions get darker. (c) The mean longitude of the RAFOS float trajectory pair vs the number of days since 1 Jan 2009 at different depths. The first day when the pair formed—when the two trajectories came within the relative separation threshold—is marked as the black dot. (d) The mean pressure of the RAFOS float trajectory pair vs the mean difference in pressure of the two trajectories, averaged over the first 100 days. (e) The number of RAFOS float pairs as a function of time conditioned on initial separation and in different depth ranges, used for the time-based metrics. (f) The number of RAFOS float pairs as a function of separation distance in different depth ranges, used for the space-based metrics. The "o" markers indicate the center of the separation bin.

vertical shear in this region is approximately $O(10^{-4})\,s^{-1}$ (Balwada et al. 2016a), which can result in a net dispersion on the order of $10\,km^2$ in 10 days and $10^3\,km^2$ in 100 days, which is negligible compared to the observed relative dispersion (Fig. 5).

The corresponding particle analysis was performed on particle pairs that were released at initial separations of 11.1 and 33.3 km. There are 20 sets of model particles released between 500 and 2000 m, and each set was composed of between 1100

and 1200 pairs. In most of the sections we focused on particles released at depths of 750 and 1500 m. These set of particles are qualitatively similar (have similar time scales and scaling relationships) to the shallow and deep sets of floats, but an exact quantitative match should not be expected. In section 3, where we quantify the variability, we selected depths that enclose the two sampled ranges, 500 and 900 m corresponding to the shallow set and 1100 and 1700 m corresponding to the deep set.

For all space-based metrics, which parse data along a separation axis ($\langle\cdot\rangle$), we defined separation bin edges as $r(n) = a^n r(0) r(n) = a^n r(0)$, where $a = 1.4$ and $r(0) = 1$ km. For floats, we only used pairs that were separated by less than 100 m in the vertical. The numbers of float pairs in each bin for the shallow and deep set are shown in Fig. 1f. The number of pairs increases from less than 100 at the smallest separation to close to 10 000 at separations of 300 km, with the deeper set having more pairs. For the particles more than 1000 pairs were available for each separation bin (not shown).

All error bars in this study are derived using the bootstrapping algorithm. We estimate the metric 1000 times, performing random draws with repetition, and use the 5th and 95th percentiles as the limits of the error bars.

3. Temporal and spatial flow variability

In this section, we quantify the distribution of the kinetic energy at different temporal and spatial scales. This will provide a helpful context to the stirring metrics that will be discussed later.

a. Rotary Lagrangian frequency spectra

Rotary spectra decompose the power in the velocity time series into counterclockwise (positive frequencies) and clockwise (negative frequencies) motions at different time scales (Thomson and Emery 2014), which correspond to anticyclonic and cyclonic motions in the Southern Hemisphere, respectively. Here we perform this spectral decomposition on the velocity following the Lagrangian trajectory, using trajectory segments of 120 days and the multitaper method (Lilly 2019).

The float rotary spectra show a plateau at low frequencies, transitioning to a power law behavior with slope of about -4 at intermediate frequencies (Figs. 2a,b). At frequencies higher than $(10 \text{ days})^{-1}$ a much flatter power law is observed. This flattening of the spectra at high frequencies can potentially be attributed to internal waves; near-inertial waves (NIWs); tides, which have been aliased to these frequencies; and some contributions from the position tracking errors. The cyclonic and anticyclonic components of the float spectra are almost indistinguishable, with no preference for a particular polarization, and the spectral energy at the shallower depths is higher than at greater depths.

At the lower frequencies, the behavior of the particle spectra is similar to the float spectra, with the low-frequency plateau from the observations lying within the range of energy levels from the model at comparable depths (Figs. 2a,b). A power law regime, with a slope of approximately -5, extends from intermediate to high frequencies. Thus, the model spectra lack the high-frequency flattening seen in the observations, which is a result of limited model resolution and the daily averaged velocities used to advect the particles.

b. Longitudinal velocity structure function

Second-order velocity structure functions represent flow correlations across spatial scales, and are related to the kinetic energy spectra (Babiano et al. 1985; LaCasce 2016). The longitudinal second-order structure function is defined as

$$S2_{ll}(r) = \left\langle (\delta \mathbf{u}(r) \cdot \hat{\mathbf{r}})^2 \right\rangle, \tag{1}$$

where $\delta \mathbf{u}(r) = \mathbf{u}(\mathbf{x} + r) - \mathbf{u}(\mathbf{x}) \delta \mathbf{u}(r) = \mathbf{u}(\mathbf{x} + r) - \mathbf{u}(\mathbf{x})$ is the velocity difference between two particles separated by distance r, $\hat{\mathbf{r}}$ is the unit vector connecting these two particles. We assume homogeneity and isotropy to drop the dependence on $\mathbf{x}$ and $\hat{\mathbf{r}}$, respectively.

The second-order longitudinal structure function is related to the longitudinal frequency–wavenumber spectrum $[E_{ll}(k, \omega)]$ via

$$S2_{ll}(r) = 2 \int_0^\infty \left[\int_0^\infty E_{ll}(k, \omega)\, d\omega \right] [1 - J_0(kr)]\, dk, \tag{2}$$

where k is the horizontal wavenumber and $J_0()$ is the zeroth-order Bessel function. Thus, $S2_{ll}(r)$ has contributions, filtered by the Bessel function, from all wavenumbers and frequencies. If the wavenumber energy spectrum follows a power law $[E_{ll}(k) = \int_0^\infty E_{ll}(k, \omega)\, d\omega \sim k^{-\alpha}]$ over a long enough range of scales and $1 < \alpha < 3$, then the integral is dominated by wavenumbers near $k \sim 1/r$ and the structure function follows a power law $[S2_{ll}(r) \sim r^{\alpha - 1}]$. While, if $\alpha > 3$ then $S2_{ll}(r) \sim r^2$ for all n (Bennett 1984; Balwada et al. 2016a). At scales where the velocities are uncorrelated the structure function is constant and equals twice the velocity variance.

Both shallow and deep float $S2_{ll}$ (Figs. 2c,d) approach a constant at scales larger than approximately 200 km, with this length scale being slightly larger for the shallower floats. The kinetic energy level, the large-scale constant value of $S2_{ll}$, observed by the shallower floats is approximately 3 times greater than the deeper floats. For the shallow floats, $S2_{ll}$ follows a power law of approximately r^1 between separation of 20 and 100 km, and becomes flatter at smaller scales. For the deep floats $S2_{ll}$ follows a power law that is slightly flatter than the shallower floats, and closer to $r^{2/3}$.

In contrast, the model structure functions are similar to those expected for a flow with a kinetic energy spectrum steeper than k^{-3}, with a power law behavior of r^2 at small scales and transitioning to uncorrelated motions at scales larger than about 100–200 km. The kinetic energy level decreases with depth similar to observations.

Thus, the structure functions also indicate energy at small scales present in the observations but not in the model. This is true for scales less than roughly 20 km and for times less than about a week.

4. Relative dispersion and kurtosis

a. Theory

The characteristics of the stirring are encoded in how the separation between particle pairs evolves, and can be

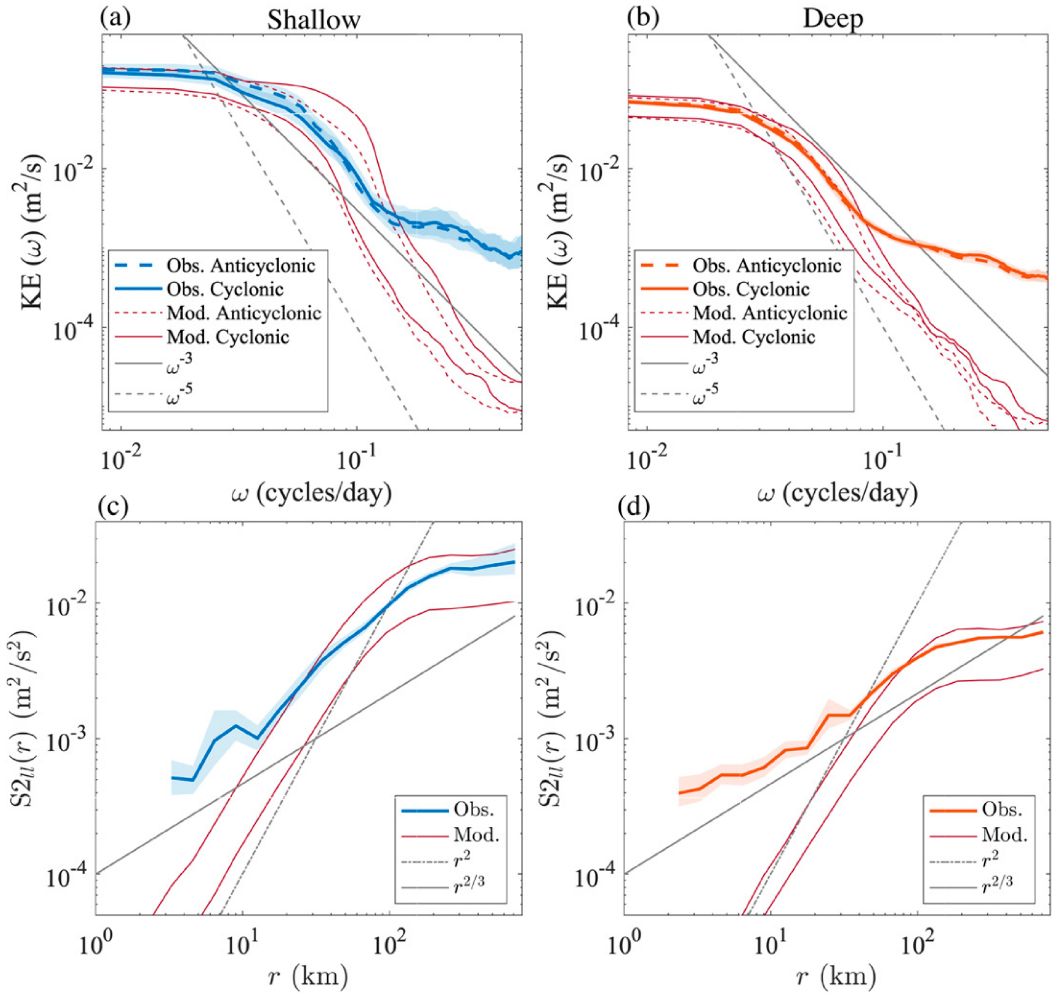

FIG. 2. Mean Lagrangian frequency rotary spectra from the RAFOS floats (a) between 500 and 1000 m and (b) between 1000 and 1800 m. The mean Lagrangian frequency rotary spectra from the model particles released at mean depths of 500 and 900 m are shown in (a), and at depths of 1100 and 1700 m are shown in (b)—the spectra at shallower depth in the model are more energetic. Power laws of ω^{-3} and ω^{-5} are also shown in (a) and (b). (c),(d) Second-order longitudinal velocity structure functions for the RAFOS floats and model particles corresponding to the same depths as (a) and (b), respectively. Power laws of $r^{2/3}$ and r^2 are also shown in (c) and (d).

quantified by considering the evolution of pair separation PDF and its moments: relative dispersion (second moment), which is a measure of the size of the tracer cloud, and kurtosis (normalized fourth moment).

The relative dispersion, the mean square pair separation, evolution can be derived using purely kinematic arguments (Babiano et al. 1990). These are based on the relative diffusivity, the derivative of the relative dispersion $\overline{r^2}$,

$$\kappa(t|r_0) \equiv \frac{1}{2}\frac{d\overline{r^2}(t|r_0)}{dt} = \langle \mathbf{r}_0 \cdot \delta\mathbf{V}(t|r_0)\rangle_{r_0} + \int_0^t \langle \delta\mathbf{V}(t|r_0)\cdot\delta\mathbf{V}(t|r_0)\rangle\, d\tau, \qquad (3)$$

where $\delta\mathbf{V}(t|r_0)$ is the relative velocity of a pair, and the dependence on the initial condition r_0 is explicitly noted. For flow randomly seeded with particles, the correlation in the first term of the RHS is typically small, as it was for both particles and floats (not shown). At short times ($t \to 0$), Eq. (3) is approximated as $\kappa(t|r_0) \approx tS2_{ll}(r_0)$, and the relative dispersion grows ballistically [$\overline{r^2} = r_0^2(1 + C_1 t^2)$], where C_1 is a constant proportional to the total enstrophy). At large times ($t \to \infty$), the relative velocities are uncorrelated [$\langle|\delta\mathbf{V}(\infty)|^2\rangle_{r_0} = 4\mathrm{KE}$]. If the integral of the time correlation of the relative velocities converges, then the relative dispersion grows linearly ($\overline{r^2} \sim t$) as for a diffusive process (Taylor 1922).

Of primary interest are the scales at intermediate times, when pair separations lie in the inertial range and pair velocities are still correlated. Here, the stirring properties can be well quantified using the pair separation PDF, from which the relative dispersion derives. The separation PDF can be

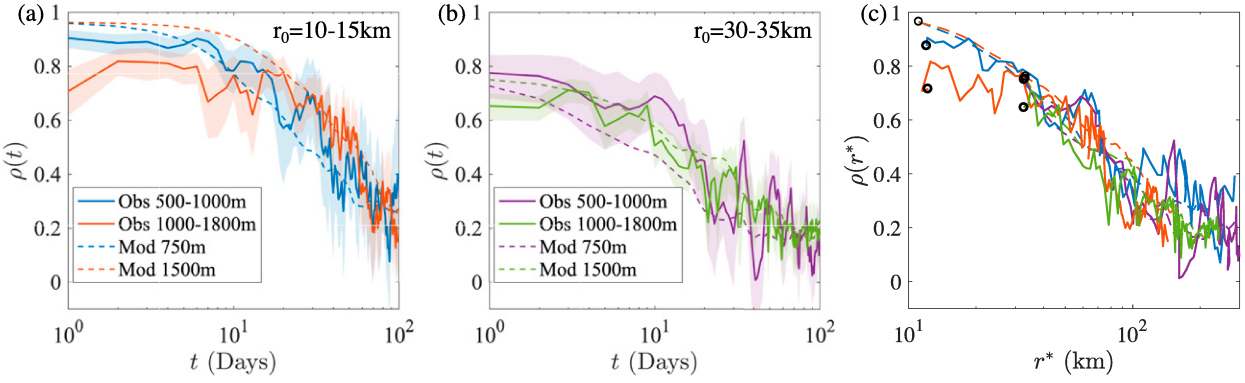

FIG. 3. Pair velocity correlations for trajectories at different depths with initial separation of (a) 10–15 and (b) 30–35 km. (c) Pair velocity correlations plotted as a function of mean pair separation [$r^* = \sqrt{r^2(t)}$] showing that correlation curves approximately collapse. Colors correspond to different depths and different initial separations as indicated in the legends, while the observational (Obs) floats are marked by solid lines and model (Mod) particles by dashed lines. Black circles mark the first day for different the correlation time series in (c).

modeled using a Fokker–Plank (FP) equation (Richardson 1926; Bennett 2006),

$$\frac{\partial}{\partial t}p = \frac{1}{r}\frac{\partial}{\partial r}\left(r\kappa\frac{\partial}{\partial r}p\right), \tag{4}$$

where $p(r, t)$ is the pair separation PDF, and $\kappa(r)$ is a diffusivity as a function of separation r. The nth raw moment of the PDF is defined as $\overline{r^n}(t) = 2\pi\int_0^\infty r^{n+1}p(r, t)\,dr$. This equation can be solved for the turbulent inertial ranges (LaCasce 2010; Graff et al. 2015), assuming all particle pairs have the same initial separation. The inertial range slope enters via the relative diffusivity [$\kappa(r)$], which can be inferred from scaling. For shallow-sloped KE spectra, where $1 < \alpha < 3$, the diffusivity scales $\kappa(r) \propto r^{(\alpha+1)/2}$, and the dispersion is characterized as "local." For steeply sloped KE spectra, $\alpha \geq 3$, the relative diffusivity scales as $\kappa(r) \propto r^2$, and the dispersion is "nonlocal." When solving the FP equation, it is assumed the same diffusivity applies across all scales. We list the analytical expressions for the PDF, the relative dispersion and kurtosis for the nonlocal regime, the Richardson regime (a particular local regime), and the diffusive regime in Table 1.

b. Correlation and isotropy from floats and particles

Correlated pair velocities are expected at scales smaller than those of the largest eddies. We define a pair velocity correlation coefficient, $\rho(t|r_0) = \langle \mathbf{u}_1(t)\cdot\mathbf{u}_2(t)\rangle_{r_0}/\langle|\mathbf{u}_1(t)|\rangle_{r_0}\langle|\mathbf{u}_2(t)|\rangle_{r_0}$, which can vary between -1 and 1. The subscripts on the velocity correspond to two members of the pair. As expected, $\rho(t|r_0)$ for floats and particles generally decreases as a function of time, and the maximum value of ρ decreases as a function of initial separation (Figs. 3a,b). Moreover, the rate of decrease is more rapid for the shallower sets than the deeper sets.

Alternatively the correlation can be visualized as a function of spatial scale by plotting $\rho(t|r_0)$ against the corresponding mean pair separation [$r^* = \sqrt{\overline{r^2}(t|r_0)}$] (Koszalka et al. 2011; Graff et al. 2015). This causes all the $\rho(r^*)$ curves to approximately collapse together (Fig. 3c), suggesting that the decrease in correlation over time is a result of pairs exiting the range of length scales over which the flow is correlated. This explains why the correlation drops more rapidly for the shallower depths, as the particles disperse faster there (seen clearly for the model particles). The collapsed curves fall below 0.5 at a length scale (r^*) of approximately 60–70 km.

Most relative dispersion theory assumes the flow is isotropic. We quantify isotropy as a ratio of the square root of the mean zonal separation to the square root of the meridional separation ($|r_x^*|/|r_y^*|$) (Morel and Larceveque 1974); this is 1 if the zonal and meridional spreading is the same. For the shallow floats and particles the ratio exceeds 1 after about 50 days (Fig. 4a) and at length scales greater than 100 km (Fig. 4c), while for the deeper sets the ratio stays close to 1 over 100 days (Fig. 4b). The only exception is the shallow float set with $r_0 \sim$ 10–15 km that shows enhanced zonal dispersion after only 10 days (though there are fewer than 50 pairs in this group). The particles always exhibit a small ratio for the first few days, which is due to the particles being deployed along a longitude line. Thus, the dispersion is nearly isotropic at scales where the velocities are correlated. Isotropy is discussed further in the section on relative diffusivity (section 5b), where we show more conclusively that the flow is isotropic at length scales smaller than approximately 100 km.

c. Relative dispersion and kurtosis from floats and particles

Due to the small number of float pairs, it is difficult to draw conclusions about PDFs themselves. The float PDFs are statistically indistinguishable from both the nonlocal and Richardson (local) theoretical PDFs (Table 1), while the particle PDFs are suggestive of nonlocal dispersion. Details are given in appendix B.

The relative dispersion increases in time, showing that on average the floats and particles disperse (Figs. 5a,d). The dispersion for the floats and particles is very similar over the first 100 days, suggesting the additional high-frequency and small-scale variability in the ocean does not contribute much to dispersion. At the shallower depth the relative dispersion increased to 300^2 km^2 by the end of the 100 days for both initial separations, while the deeper relative dispersion was smaller. Toward

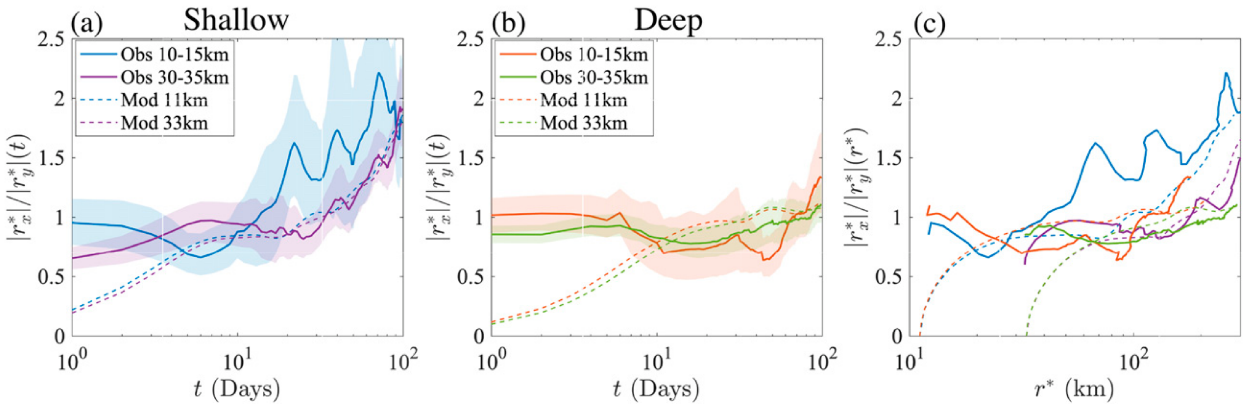

FIG. 4. Isotropy, defined as ratio of mean zonal separation to mean meridional separation for pairs at different depths—(a) shallow and (b) deep—and for different initial separations. (c) Isotropy ratio plotted as a function of mean pair separation r^*.

the end of the 100 days the dispersion for most sets has transitioned to a diffusive linear growth.

Under Richardson dispersion, the relative dispersion would grow cubically in time. However, this asymptotic limit likely cannot be achieved in the ocean because of the finite size of the inertial ranges, and would likely not be reflected in the data. So to study the relative dispersion before the asymptotic limit is reached, an expression for the Richardson dispersion at all times was derived in Graff et al. (2015) (presented in Table 1); this expression is relatively complex. However, we found (not shown) that the less rigorous but simpler expression, $(r_0^{2/3} + C_2 t)^3$, derived by Ollitrault et al. (2005) is visually indistinguishable from the more complex expression of Graff et al. (2015), when both are plotted in a compensated form: $\overline{r^2}^{1/3} - r_0^{2/3}$. This form, based on the expression from Ollitrault et al. (2005), removes the dependence on initial condition and has a slope

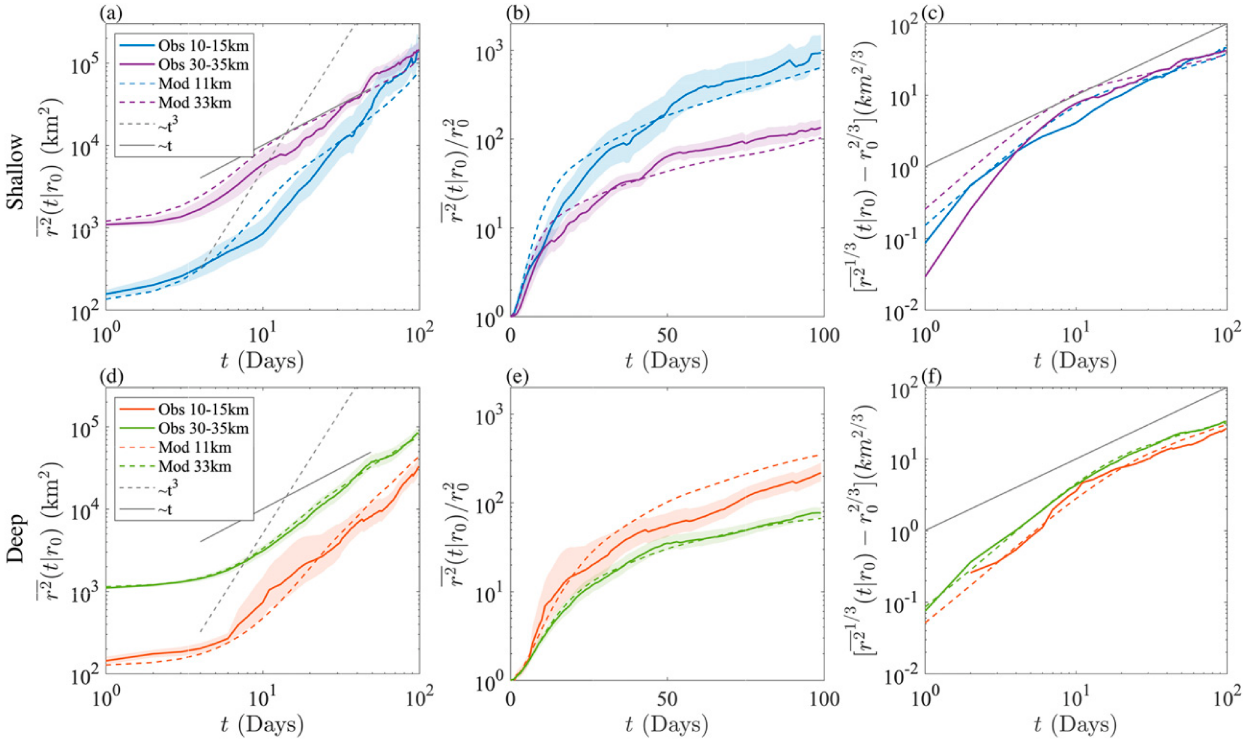

FIG. 5. Relative dispersion as a function of time for different r_0 and at different depths from the floats (solid lines) and particles (dashed lines). (top) Shallow sets and (bottom) deep sets, where different colors correspond to different sets as indicated in the legends that are shared between panels: (a),(d) the dispersion on a log–log axis; (b),(e) the dispersion normalized by the initial dispersion on a semilog axis for ease of comparison to nonlocal dispersion; and (c),(f) the dispersion in a compensated form as indicated in the axis label for ease of comparison against Richardson dispersion. The gray lines correspond to the linear (solid) and cubic (dashed) power laws.

of one on a log–log plot under Richardson dispersion. The compensated relative dispersion from the floats and particles, using the compensated form, not show a distinct linear range (Figs. 5c,f). Generally, the growth rate is faster than the expectation from Richardson dispersion initially and then slower. A short range from approximately 6–20 days for the shallower sets and 15–30 days for the deeper sets shows a growth rate that might be comparable to Richardson dispersion, but it is more likely that this is simply a transition period. The shallow float set with $r_0 \sim 10$–15 km is a slight exception, since it approximately matches with Richardson dispersion from 2 to 40 days (also true for kurtosis discussed next). As noted though this set has few pairs, and thus the approximate match to Richardson dispersion may not be robust.

If the dispersion were nonlocal, it would grow exponentially in time. The relative dispersion, for both floats and particles, increases rapidly for the first 10–25 days and then settles into a slower growth afterward (Figs. 5b,e). The initial growth is not distinguishable from exponential. For example, the relative dispersion for the shallow particles with $r_0 = 11$ km between 4 and 15 days suggests that exponential growth occurs up to approximately length scales of $\sim 5r_0 \approx 55$ km. Similar phases of exponential growth are also seen at other depths for the particles, and to some degree for the floats. This rapid growth ends when the mean separation reaches $r^* \sim 50$–90 km for all cases considered, and is thus shorter for larger r_0. The relative dispersion from the particles for the first 3–4 days shows a slightly slower growth rate, which is likely a result of dependence on initial conditions and a short phase of ballistic growth (see further discussion in appendix B).

Under nonlocal dispersion, the kurtosis also grows exponentially, while it asymptotes to 5.6 under 2D Richardson dispersion; it asymptotes to 2 if the dispersion is diffusive (Table 1) (LaCasce 2010). Local dispersion with a spectral slope between -3 and $-5/3$ can also result in kurtosis surpassing 5.6 (Foussard et al. 2017).

The kurtosis from the floats and particles evolves similarly, with a rapid initial increase for approximately 10–20 days followed by a decay toward 2 (Fig. 6). The kurtoses do not rise to very large values because r_0 is large. The pairs in the tails of the PDFs transition to the uncorrelated regime at about 10–20 days (Fig. B1), so that the kurtosis could not rise to large values even under exponential initial growth. Thus, one cannot distinguish local or nonlocal dispersion at small scales based on the kurtosis. But the similarity between float and particle kurtoses suggests the floats disperse similarly to the particles.

Thus the pair separation moments from the floats and particles are similar within the errors. However, it is difficult to distinguish the exact type of dispersion occurring at small scales. This is likely due to the relatively large initial separations r_0. Next we consider space-based metrics, which average without any conditioning on r_0.

5. Relative diffusivity

Now we examine the relative diffusivity. The initial separation r_0 is used to assign the spatial scale, so that $\kappa(r) \approx \kappa(t|r_0)$ [Eq. (3)]. We estimate $\kappa(r)$ using finite difference,

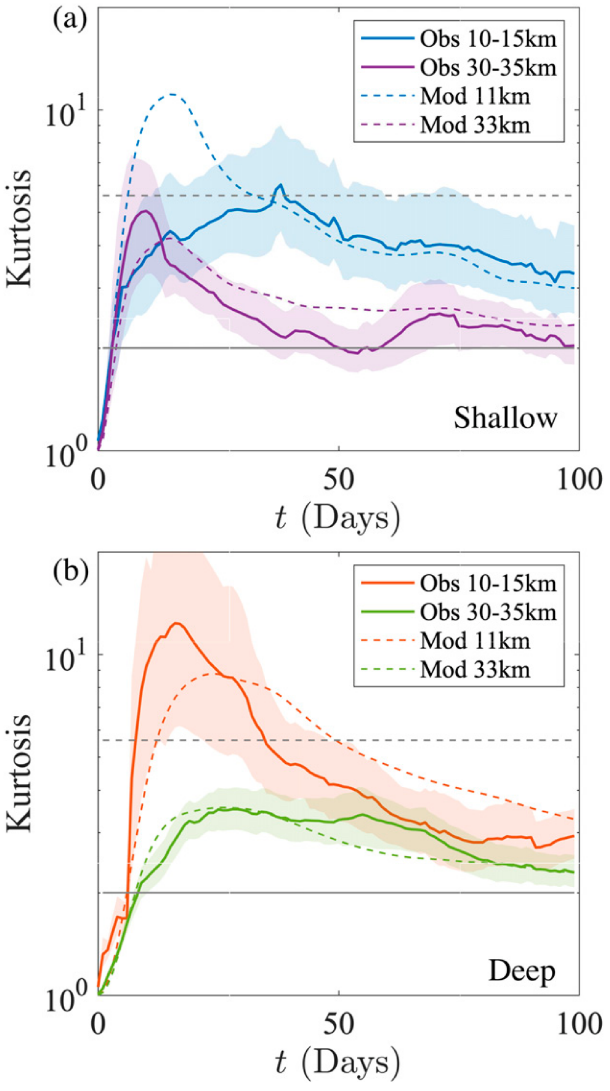

FIG. 6. Kurtosis ($\overline{r^4}/\overline{r^2}^2$) as a function of time for the floats (solid lines) and the particles (dashed lines) for different r_0 and depths: (a) shallow sets and (b) deep sets, and different colors correspond to different sets as indicated in the legends. The horizontal lines correspond to the kurtosis for Richardson dispersion (5.6, dashed line) and simple diffusion (2, solid line).

$$\kappa(r) = \kappa(\Delta t/2|r_0) \approx \frac{d\overline{r^2}(\Delta t/2|r_0)}{dt} \approx \frac{\overline{r^2}(\Delta t|r_0) - \overline{r^2}(0|r_0)}{\Delta t}. \quad (5)$$

It is possible to use different time spacings, Δt, which we will vary to estimate the longer time estimate of relative diffusivity and to filter high-frequency motions in the observations. The time spacing should also be small enough so that the diffusivity is less than the asymptotic value of twice the single particle diffusivity (LaCasce 2008). The single particle integral time scale for the region is approximately 5–6 days (Balwada et al. 2016b); as discussed below, this works well as a practical estimate of Δt. Further consideration about the link between second-order structure function and relative diffusivity, effects

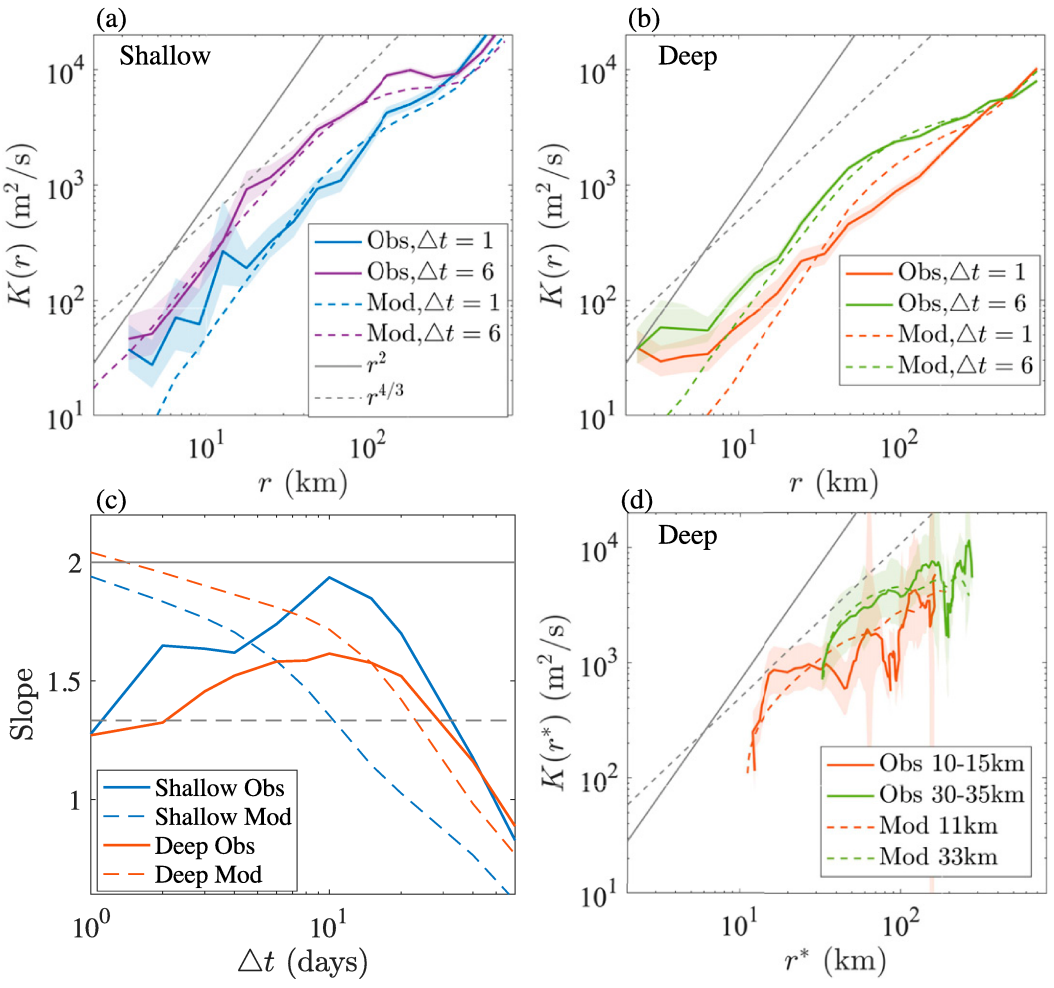

FIG. 7. Relative diffusivity as a function of separation scale. (a) Shallow and (b) deep estimates of $\kappa(r)$, for the floats and particles with Δt of 1 and 6 days. (c) Slope of the relative diffusivity curve between 6 and 50 km as a function of Δt. The horizontal gray lines are the values of the slope corresponding to nonlocal (2; solid) and Richardson (4/3; dashed) dispersion. (d) Relative diffusivity estimated as $\kappa(r^*, r_0)$ for the deep floats and particles, with Δt of 6 days. The gray lines correspond to the power laws expected for nonlocal (solid) and Richardson (dashed) dispersion. The position of these gray lines is the same in the three panels [(a), (b), and (d)] and can be used to compare the estimates more easily.

of the high-frequency motions, and theoretical guidance for varying Δt is given in appendix C.

We first examine the dependence of $\kappa(r)$ on Δt using the model particles. The diffusivities for the shallow and deep particles with $\Delta t = 1$ day increase as r^2, up to scales of approximately 50–60 km, in line with a steep spectrum. At larger scales the diffusivity flattens out. At still larger scales, the diffusivity increases again, approximately as $r^{4/3}$ (Fig. 7a). The slope of the power law dependence for the particles between 6 and 50 km is not very sensitive to Δt up to moderate values, ~6 days for shallow and ~10 days for deep particles, but flattens out with larger Δt. This follows as pairs with smaller r_0 start to experience more uncorrelated motion and the relative diffusivity asymptotes to the large-scale diffusivity, flattening the slope (Fig. 7c). Increasing Δt to 6 days increases the magnitude of the diffusivity for separations between 6 and 50 km, because at 6 days the pairs are sampling larger scales than r_0 with larger diffusivities, but this does not change the power law dependence significantly. The choice to plot the results hereafter using 6 days is a pragmatic one; the slope of the relative diffusivity of the shallow particles is not very sensitive within this time frame, and 6 days is similar to the single particle integral time scale for the floats in this region.

The float-derived diffusivities exhibit a different dependence on Δt (Figs. 7a–c). With $\Delta t = 1$day, $\kappa(r)$ exhibits a power law dependence close to $r^{4/3}$ at scales smaller than 100 km. This is consistent with $S2_{ll}(r)$ being flatter, as shown in section 3 [$\kappa(r, t) \approx tS2_{ll}(r)$ at short times (Babiano et al. 1990)]. As Δt is increased, the power law steepens (Fig. 7c), and over a range of intermediate values of Δt agrees well with the power law of the particle diffusivity down to scales of 5km. This suggests increasing Δt acts as a filter, removing the high-frequency motions

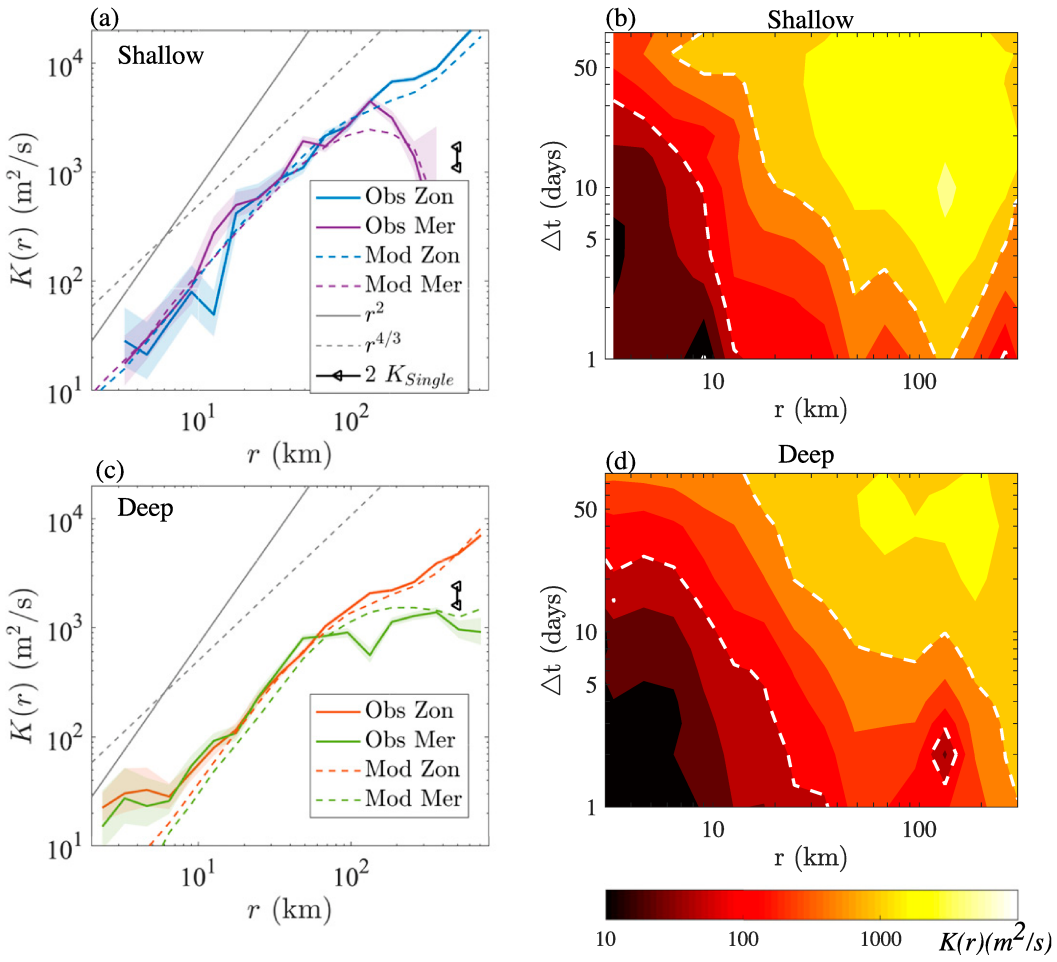

FIG. 8. The zonal and meridional relative diffusivity $\kappa(r)$ for the (a) shallow and (c) deep floats and particles, estimated with Δt of 6 days. The short black line at 500 km corresponds to twice the single particle diffusivity from Balwada et al. (2016b). The gray lines correspond to the power laws expected for nonlocal (solid) and Richardson (dashed) dispersion. The meridional relative diffusivity for the (b) shallow and (d) deep floats as a function of separation and Δt is contoured. Values of 100 and 1000 $m^2 s^{-1}$ are contoured using dashed white lines.

that cause the relative diffusivity power law from the floats to be flatter than that of the particles at short times. As with the particles, when Δt is increased further ($\Delta t > 15$ days) the slope flattens, as the influence of the uncorrelated scales becomes more dominant. It should be noted that a perfect match between the relative diffusivity slope dependence on Δt from floats and particles at these longer Δt should not be expected, because the floats are spread over a depth range and the particle depths were chosen to only match the float depth approximately (section 2).

Thus, the high-frequency motions present in the observations are responsible for the diffusivity's weaker dependence on r (local dispersion) when the evolution of the pairs over a short time period is considered. However, the diffusivity's dependence on r steepens (nonlocal dispersion) when the evolution of the same pairs over a few days is considered; indicating that the smaller scales have a relatively weaker net impact as some of the higher-frequency pulsation in separation averages out to zero. We find that wave-like motions are a likely process that can result in this observed behavior for the relative diffusivity, as detailed in appendixes A and C.

As the mean flow here is nearly zonal (LaCasce et al. 2014; Balwada et al. 2016a), the zonal and meridional diffusivities reflect the stirring along and across the mean flow. Using the longer time spacing ($\Delta t = 6$ days), the zonal and meridional diffusivities for the floats and particles are very similar, suggesting isotropy up to roughly 100 km separations (Figs. 8a,c). At larger scales, the zonal and meridional diffusivities diverge as the flow becomes anisotropic and pair velocities are uncorrelated. The zonal diffusivity continues growing with a scaling close to $r^{4/3}$. This anisotropic growth could be indicative of shear dispersion (Bennett 1984; LaCasce 2008). At these scales of uncorrelated motion the meridional diffusivity approaches a constant value close to twice the single particle diffusivity estimate for the region (LaCasce et al. 2014; Balwada et al. 2016b). At the correlated scales, the meridional relative diffusivity is an increasing

function of separation scale and time scale (Δt) and is greater at the shallower depth (Figs. 8b,d).

Some studies [e.g., Sinha et al. (2019) and Sansón (2015) most recently], estimate the scale dependence of relative diffusivity by differentiating the relative dispersion time series for a particular initial separation and assigning the mean separation $[r^*(t)]$ as the spatial scale $[\kappa(r^*|r_0)]$. Using this estimate (Fig. 7d), we were even unable to detect r^2 regime for the particles, possibly since the average occurs over a wider range of scales. This estimate was very noisy for the floats.

6. Finite size Lyapunov exponents

a. Theory

Finite size Lyapunov exponents are an alternate way of quantifying stirring, and measures the average time taken $[\tau(r)]$ for a pair of particles to grow in separation from scale of r to ar, where $a > 1$ (Artale et al. 1997). FSLE (λ) is defined as

$$\lambda(r) = \frac{\log(a)}{\langle \tau(r) \rangle}. \tag{6}$$

Theoretical scalings for FSLE can derived based on turbulent scaling arguments. If the stirring is local and the energy spectrum follows a power law of $k^{-\alpha}$ ($\alpha < 3$), then the FSLE scales as $\lambda(r) \propto r^{(\alpha-3)/2}$. Thus, for Richardson dispersion the FSLE scales as $\lambda(r) \propto r^{-2/3}$. For $\alpha \geq 3$, the FSLE converges to a constant $[\lambda(r) \propto r^0]$, and for uncorrelated diffusive spreading $\lambda(r) \propto r^{-2}$. These are summarized in Table 1.

b. FSLE from floats and particles

The floats were tracked daily, and the output of the particles was saved daily. This sets an artificial discretization on the possible values of λ, which would particularly be an issue at smaller r when particle pairs will separate to ar in one or two time steps. To alleviate this issue, we linearly interpolated the separation time series between the resolved times (LaCasce 2008; Lumpkin and Elipot 2010; Haza et al. 2014). The interpolation caused an increase in the value of the FSLE for floats, and also slightly steepened the power law behavior at smaller scales (not shown). The linear interpolation also increases the value of FSLE slightly for the particles, but does not change the power law behavior of FSLE (not shown). The FSLE estimated using the linear interpolation was not sensitive to the size of the bins (value of a, which is chosen to be 1.4 here).

The FSLE from the floats shows an approximate $-2/3$ dependence at scales smaller than 100 km, at both the shallow and deep levels (Fig. 9). At scales larger than 100 km the FSLE slope becomes steeper, tending toward -2. The FSLE from the particles at scales smaller than 100 km is almost flat, and markedly different from the floats. At scales greater than 100 km the FSLE from particles is almost identical to that from floats. At the shortest scales, smaller than the model resolution, the particle FSLE slightly diverges from a constant, which is presumably a result of interpolation used in particle tracking. There is no qualitative difference between the results of the shallow and deep sets, except for the time scales being faster at shallower depth.

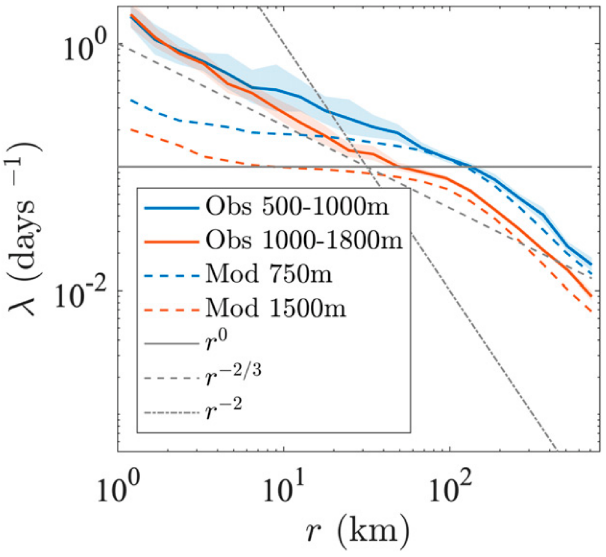

FIG. 9. Finite scale Lyapunov exponents as a function of scale for the shallow and deep sets of trajectories from the floats (solid line) and particles (dashed line). The dashed lines correspond to different theoretical expectations: nonlocal (r^0), Richardson ($r^{-2/3}$), and simple diffusion (r^{-2}).

The results suggest the floats experience local dispersion and the particles nonlocal dispersion at scales smaller than 100 km. Both exhibit diffusive spreading at larger scales. The time scale associated with the FSLE at small scales is 1–10 days, which is where the high-frequency motions appear in the observations (section 2). So these motions are likely associated with the local dispersion seen here.

We consider the effects of high-frequency motion on the FSLE further in appendix A. We show that wave energy at time scales shorter than a day can be aliased to scales of 1–10 days when the temporal resolution is a day; and this aliased energy can potentially cause the FSLE to appear local even when the dispersion is a result of nonlocal stirring. Thus, we cannot conclude based on the float FSLE that the dispersion is local, but the characterization of the particle FSLE being nonlocal is appropriate.

7. Discussion

The southeast Pacific Ocean sector of the ACC, between the East Pacific Rise and Drake Passage, was sampled by a subset of DIMES RAFOS floats and simulated with an eddy-permitting model. We provide an observational perspective on turbulent stirring in the ACC at length scales comparable to and smaller than the mesoscale eddies, in one of the few observational studies that addresses relative dispersion in the deep ocean. The stirring is quantified using time-based and space-based metrics (summarized in Table 2).

At scales comparable to and larger than the mesoscale eddies the pair velocities are uncorrelated, and the dispersion is anisotropic. The meridional dispersion behaves like random walk and zonal dispersion behaves like shear dispersion. The

meridional relative diffusivity saturates at a value near $1000\,m^2\,s^{-1}$, in agreement with single particle-based estimates (Balwada et al. 2016b; LaCasce et al. 2014; Tulloch et al. 2014). This is approximately two orders of magnitude larger than the relative diffusivity at scales smaller than 10 km, in agreement with the estimates based on DIMES tracer roughness (Boland et al. 2015).

At scales smaller than the mesoscale eddies the pair velocities are correlated, and the dispersion is isotropic. Under these conditions the stirring can be characterized as local, primarily influenced by eddies at the scales of the pair separations, or nonlocal, primarily influenced by eddies that are much bigger than the scales of the pair separations. Overall, we concluded that the RAFOS floats likely experienced nonlocal stirring at scales longer than a few inertial periods and at approximately 5–100 km in this part of the ocean, since at these scales their dispersion is broadly similar to that of nonlocally dispersed model particles. However, some important distinctions between the different time- and space-based metrics for the floats and particles are present.

The time-based metrics, relative dispersion and kurtosis, for the floats and particles are broadly consistent, but neither floats nor particles could conclusively categorize the stirring as local versus nonlocal. This consistency is not completely expected, since the Lagrangian frequency spectrum and second-order structure functions indicated that the floats experienced a flow field that was more energetic than the model, at scales less than roughly a week and 20–30 km. The main issue with the time-based metrics was that in an effort to have a sufficient number of samples, a relatively large initial separation had to be selected. Having a large initial separation results in the pairs dispersing to the uncorrelated scales relatively fast, which does not allow the distinct signatures of the dispersion regimes to emerge very prominently.

The space-based metrics, relative diffusivity and FSLE, indicated that the dispersion is local for the floats and nonlocal for the particles, when these metrics are computed at the sampling time scale of 1 day. For the relative diffusivity, which allows integration in time, we found that after integrating over time scale of 6 days the relative diffusivity from the floats had the same characteristics as the relative diffusivity from the particles at scales larger than 5 km. This suggests that the highest-frequency motions have little or no impact on dispersion. It is not possible to say from float trajectories alone, but it is likely that the high-frequency range is dominated by NIWs, internal wave continuum, and tides. Independent observations suggest these high-frequency flows are abundant in the ACC (e.g., Ledwell et al. 2011; Waterman et al. 2013; Kilbourne and Girton 2015). Despite having superinertial frequencies, this wave energy can be aliased into the float positions, which are sampled once a day. We showed in appendix A that adding linear waves, which do not add any particle dispersion, to the nonlocally dispersed model particle trajectories can make the space-based metrics to appear local at length scales that are 20–30 times the displacement amplitude of these waves. Integrating the relative diffusivity in time is found to be a practical way to recover the underlying dispersion characteristics.

Linear waves have relatively little effect on lateral stirring of Lagrangian particles (Holmes-Cerfon et al. 2011), but they can cause appreciable stirring for a tracer that can diffuse diapycnally (Young et al. 1982). Previously it was shown that inertial oscillations have a similar minimal effect with surface drifter pairs, contributing substantial energy to the structure functions at small scales without impacting lateral dispersion (Beron-Vera and LaCasce 2016). Local stirring at small scales has been observed in several studies, most comprehensively in the global drifter study of Corrado et al. (2017). The evidence for this usually comes from space-based metrics. While it is certain that superinertial motions affect energy spectra at submesoscales, it remains to be seen to what extent these motions affect lateral dispersion. At least in the present case, the effect appears to be small.

Our conclusion of nonlocal dispersion from the floats is also consistent with the behavior of the tracer released during the DIMES experiment, which showed small irreversible diffusivity during the initial filamentation phase up to the scales of the mesoscale eddies, and growing irreversible diffusivity after the tracer filaments start to merge and form a large tracer cloud (Zika et al. 2020). This is in line with the characteristics of stirring and filamentation in the deep ocean that was hypothesized by Garrett (1983), and has also been observed in the North Atlantic during the North Atlantic Tracer Release Experiment (NATRE; Sundermeyer and Price 1998).

We cannot entirely discount the possibility that small-scale flows in the interior ocean can lead to some net dispersion, particularly at the smallest scales ($<$10 km), and the true dispersion might be in some sense weakly local at these smaller scales. Some recent studies have identified that submesoscale flows with surface origins can penetrate appreciably below the mixed layer (Yu et al. 2019; Siegelman 2020). Strong submesoscale flows and eddies in interior ocean, without any surface association, can also potentially result from interaction between internal waves and balanced flows (Thomas and Yamada 2019), or result due to breaking waves creating mixed patches that then coalesce into pancake vortices due to an inverse cascade (Sundermeyer et al. 2005; Polzin and Ferrari 2004), or be generated by flow interacting with topography and spinning off eddies (Srinivasan et al. 2019; Vic et al. 2018; Bracco et al. 2016). It is also possible that isobaric floats, which do not follow water parcels in the vertical, can disperse away from the water parcels that they were originally tracking (Dewar 1980). However, it seems that the influence of these small-scale flows, if they are present, does not appear as a first-order effect in the metrics and at the scales considered here, and if these scales are causing any significant stirring then it is not easily distinguishable from sampling noise and biases. Hence, it is also important to devise new metrics that will be more sensitive to the stirring at smaller scales.

Most current ocean models use diffusive parameterizations (Fox-Kemper et al. 2019), even at scales where the stirring is not diffusive. Our hope is that the present observations will inspire new stirring parameterizations (e.g., Kämpf and Cox 2016), along with efforts in improvement of parameterizations of ocean energetics (Bachman et al. 2017; Zanna 2019), for ocean models that partially resolve mesoscale eddies.

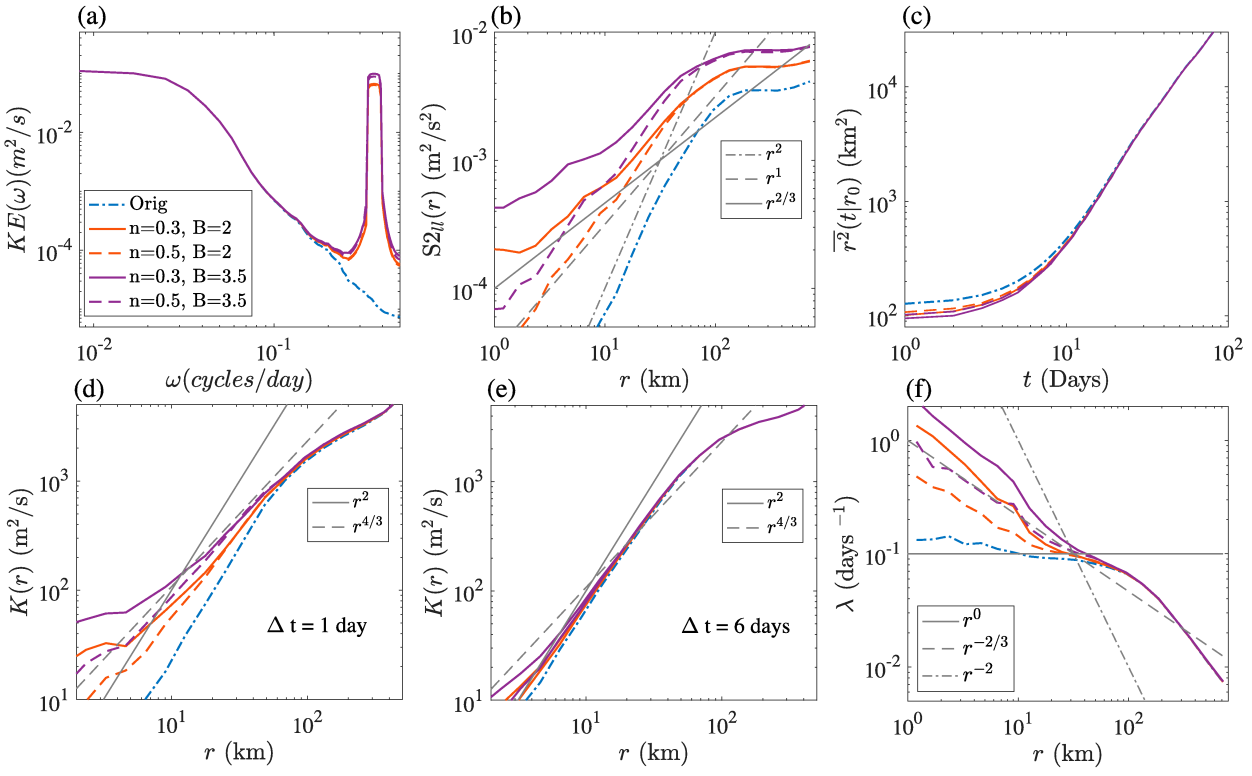

FIG. A1. The impact of adding monochromatic waves with inertial frequency to model trajectories on different metrics: (a) Lagrangian frequency spectrum, (b) longitudinal structure function, (c) relative dispersion, relative diffusivity with (d) $dT = 1$ day and (e) $dT = 6$ days, and (f) FSLE. All plots have data from five sets of trajectories: the original trajectories at a depth of 1500 m and the same with added waves of different spatial properties, as noted in legend in (a). In (b), (d), (e), and (f) some lines corresponding to standard scalings are also added in gray.

Acknowledgments. DB and KS acknowledge support from NSF OCE 1658479 and NSF OCE 1231803, and DB also acknowledges additional support from NSF OCE 1756882. JHL was supported by by the Rough Ocean project number 302743 under the Norwegian Research Council. The code for all the analysis and figures is shared at https://github.com/dhruvbalwada/mesoscale_stirring_dimes_floats, the RAFOS float dataset is made publicly available by NOAA/AOML at https://www.aoml.noaa.gov/phod/float_traj/data.php, and the processed data can be made available at request to the corresponding author.

APPENDIX A

Impact of Linear Waves on Space-Based and Time-Based Metrics

Recent studies have shown that the space-based stirring metrics, which average the data into spatial bins, can sometimes result in misleading conclusions in the presence of linear waves, which do not cause any net particle dispersion (Beron-Vera and LaCasce 2016), or position errors in trajectories (Haza et al. 2014). For completeness, and because neither of the previous studies considered all the metrics together, here we demonstrate the biases in conclusions about the stirring regime that can occur if monochromatic waves are added to the particle trajectories.

We modified the position vectors of the particle trajectory pair members ($\mathbf{X}_i$ and $\mathbf{X}_j$) by adding oscillations with a single frequency,

$$\mathbf{X}_i \rightarrow \mathbf{X}_i + A[\sin(\omega t + \phi), \cos(\omega t + \phi) - 1],$$
$$\mathbf{X}_j \rightarrow \mathbf{X}_j + [A + Bg(r)][\sin(\omega t + \phi), \cos(\omega t + \phi) - 1]. \quad \text{(A1)}$$

Here A is the amplitude of the oscillation common to both members, and B is the difference in the amplitude for the pair member, with the function $g(r)$ depending on pair separation ($r = |\mathbf{X}_i - \mathbf{X}_j|$). The term ω is the frequency, and ϕ is the starting phase of the waves. The function $g(r)$ models the change in amplitude as the particles move away from each other. The function $g(r)$ is modeled as a power law with slope n below a length scale r_L and a constant at larger scales,

$$g(r) = \left(\frac{r}{r_L}\right)^n, \quad \text{for} \quad r < r_L, = 1, \quad \text{for} \quad r \geq r_L. \quad \text{(A2)}$$

Beron-Vera and LaCasce (2016) employed a similar function in time rather than space, to mimic inertial oscillations in the Gulf of Mexico. The variables A and B are prescribed as random numbers from a uniform distribution that can vary between 0–$2A_{\max}$ and 0–$2B_{\max}$. The starting phase ϕ was

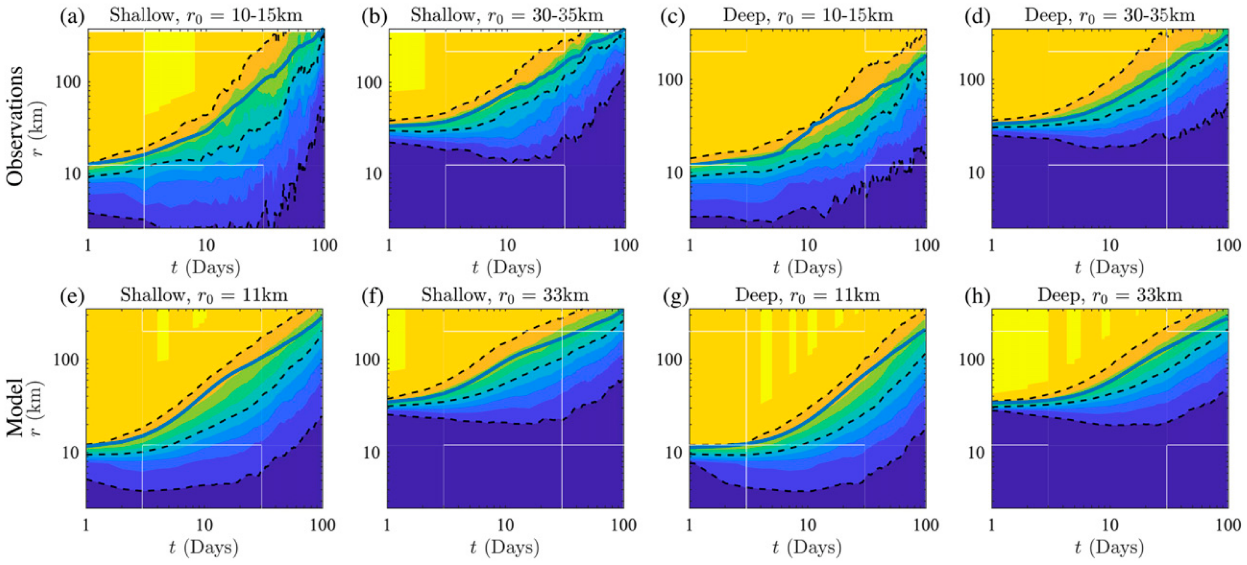

FIG. B1. Pair separation cumulative distribution functions for the (a)–(d) floats and (e)–(h) particles. Each panel corresponds to a different depth and different r_0, as indicated in the panel titles. The contour color bar ranges from 0 to 1, with increment steps of 0.1. The 0.1, 0.5, and 0.9 contours are marked with dashed black lines, while the mean pair separation is the solid blue line.

chosen as a random number on the interval $(0, 2\pi)$. The frequency ω was set to the local inertial frequency. We experimented with different choices of the parameters ($A_{\max}$, $B_{\max}$, n, r_L), and here we show results for four cases with physically reasonable values: $A_{\max} = 1.5$ km, $r_L = 50$ km, $B_{\max} = 2$ and 3.5 km, and $n = 0.3$ and 0.5. These values result in waves that are reasonably close in magnitude to the NIWs measured in the same region and during the same time as the floats (Kilbourne and Girton 2015). Since the waves are monochromatic and the inertial frequency $[\sim 1\ (14\,\mathrm{h})^{-1}]$ is greater than the sampling frequency $[\sim 1\ (24\,\mathrm{h})^{-1}]$, the frequency spectrum shows a peak in a narrow band at a lower-frequency where most of the wave signal has been aliased (Fig. A1a). We do not expect such a pronounced peak in the observations because the waves in the ocean are spread over a wider frequency range.

The space-based stirring metrics estimated using the modified trajectories are qualitatively different from those estimated using the original trajectories (Figs. A1b,d,f). The addition of waves impacts the metrics significantly, with the range of influence depending on the strength and spatial correlation of waves. For example, the FSLE for $n = 0.5$ and $B = 3.5$ km (dashed purple line in Figs. A1f), indicates local dispersion up to scales that are ~20–30 times larger than the relative amplitude of the waves. Thus, high-frequency motions due to linear waves preferentially impact the space-based metrics.

The time-based metrics are less affected: the relative dispersion (Fig. A1c), the separation PDFs, and kurtosis (not shown). This is because the added oscillations cancel out when integrated over time, with the integration time depending on the noise magnitude; Fig. A1c shows that it takes approximately 5–8 days for the wave contributions to integrate out of the relative dispersion with $r_0 = 11$ km. This initial influence on relative dispersion influences the relative diffusivity–$\kappa(r)$ (Fig. A1d) when Δt is small. However, waves can be filtered by increasing the Δt used to estimate the time derivative (Fig. A1e), which allows for recovering the sub-inertial signal. We used the same filtering method in section 5.

The objective here was not to develop a realistic model for the wave effects on the trajectories, but to simply show that wave motions that do not disperse particle pairs can easily impact some metrics commonly used to the infer the characteristics of pair dispersion. Further, this is meant to be an Occam's razor approach—if all the small-scale motions absent in the model were represented using only waves that do not disperse particles, could they make the metrics from the model looks similar to the observations within realistic ranges of wave parameters?

APPENDIX B

Separation PDFs and Initial Evolution of Separation from Floats and Particles

The pair separation PDFs provide direct insight into how the turbulent flow stirs and disperses floats and particles. For easier visualization we show the cumulative distribution function (CDF), which is monotonic and varies between 0 and 1.

Qualitatively the evolution of the CDFs from the floats and particles is very similar (Fig. B1). Only a small distinction is seen in the initial behavior, when the float CDFs are wider than the particle CDFs, which is simply a result of the float pairs having a spread over the initial separation bin. During the first 5–10 days the pair separations spread to both larger and smaller scales than r_0, and after this the pair separations increase on average as the trajectory clusters get more dispersed. Also during the initial phase the mean pair separation (r^*) coincides with the separation where the CDF is around 0.8–0.9, indicating that the long tails of the PDF are responsible for

controlling the mean pair separation or dispersion. As time progresses r^* starts to coincide more with smaller values of the CDF (≈0.5–0.6), as is expected for diffusive pair separation. Also, at most times during the evolution the pairs occupy 1–2 decades of spatial scales, suggesting that the pairs potentially sample many different turbulent regimes, and the PDFs might only evolve like the theoretical solutions for short periods of time.

We compare the PDFs of the float and particle pairs with the different theoretical solutions using the two sample Kolmogorov–Smirnov (KS) test, which is used to test the null hypothesis that the data from two sets of samples comes from the same continuous distribution (Berger and Zhou 2014). It returns a KS statistic or p value, where a large p value (>0.05) suggests that the null hypothesis cannot be rejected, implying that the two sets of samples might have been sampled from the same distribution. Here our first sample set was the separations measured by the float or particle pairs, while the second sample set was 10 000 randomly generated samples using the theoretical PDF (equations in Table 1).

To generate the random samples from the theoretical PDFs, and compare against the float and particle PDFs, we need two parameters: r_0 and the growth parameters—β for the Richardson or T_L for the nonlocal dispersion. We do not assume a priori that one regime is a better descriptor than the other, instead we estimate the growth parameters corresponding to both regimes and then use the KS test to check how well do both the theoretical PDFs with the estimated parameters match the measured separation PDF.

The parameter estimation is done by fitting the different theoretical relative dispersion (equations in Table 1) to the relative dispersion measured by the floats and particles (discussed in section 4d). Similar fittings to estimate parameters were done by Graff et al. (2015) and Beron-Vera and LaCasce (2016), where the fitting was done over the time period it took for the mean separation to increase to some chosen multiple of the initial separation. Here instead of fitting over a specified period, we fit over a range of times, and test the sensitivity of the parameters and PDF matching between theory and measurements to the choice of the duration over which the fit is done. We fit both the theoretical curves during the period between day 0 and day t_a, where t_a ranges from 3 to 50 days, using least squares fitting. The parameters are estimated even if the theoretical curve is a poor fit to the dispersion, but since these parameters also give a poor fit to the PDF they are ruled out by the KS test. Using these estimated parameters (Fig. B2) we calculated the KS statistic to compare the measured PDFs against theoretical PDFs (Fig. B3).

The comparison of the float PDFs to the theoretical PDFs suggests that for much of the time the PDFs measured by the floats could correspond to both the Richardson and the nonlocal PDF (Fig. B3), as t_a is varied. This result is particularly relevant when r_0 = 10–15 km. The deep float set released with initial r_0 = 30–35 km is a notable exception; for t_a > 20 days a match to nonlocal regime is seen for approximately 10 days followed by a Richardson regime from approximately 10 to 70 days (Figs. B3d,l). This suggests nonlocal stirring up to scales of 50km and Richardson like stirring at scales larger than 50 km, where the length scale estimate is based on the mean

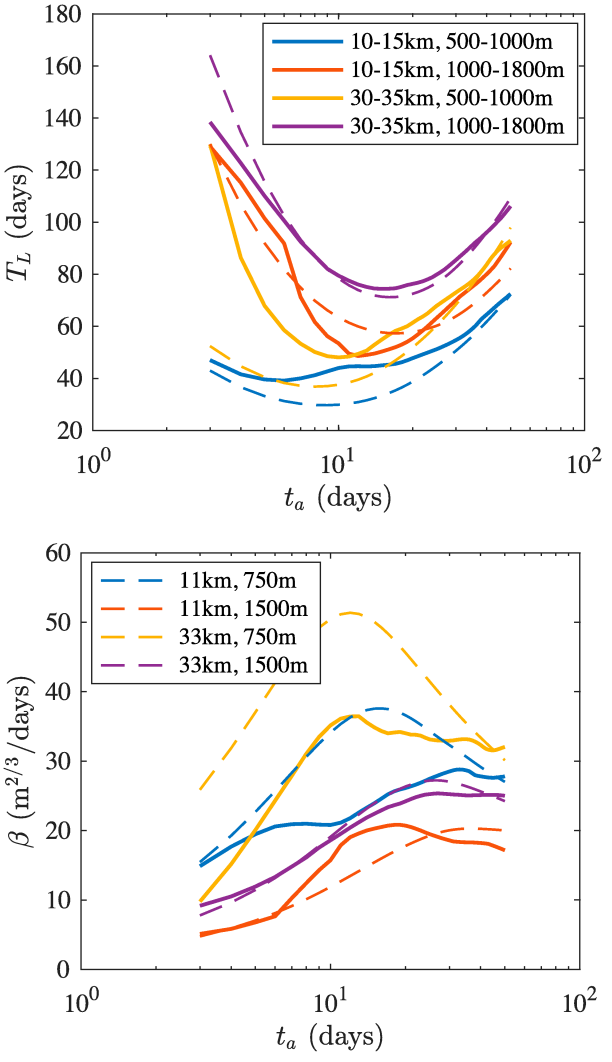

FIG. B2. Theoretical parameters (a) T_L and (b) β estimated by fitting measured relative dispersion with theoretical relative dispersion (Table 1). Different depths and initial separations are indicated by colors, while the parameters estimated using floats are marked by solid lines and the parameters estimated using the particles are marked by dashed lines. Panels (a) and (b) share their legends.

separation curve in Fig. B1d. A similar, but relatively less well defined behavior is also seen for the shallow float set released with the same initial r_0 (Figs. B3b,j).

A comparison of the particle PDFs to the theoretical PDFs shows different behavior compared to the float PDFs. The particle PDFs are better determined due to having significantly larger number of samples (>1000 pairs), which results in very short periods over which the measured particle PDFs comply with any of the two theoretical PDFs. All combinations of r_0 and depths considered here show a range where the corresponding particle PDF matched with the theoretical PDF for nonlocal dispersion (Figs. B3e–h). The Richardson PDF does not match the particle PDF at either of the depths for

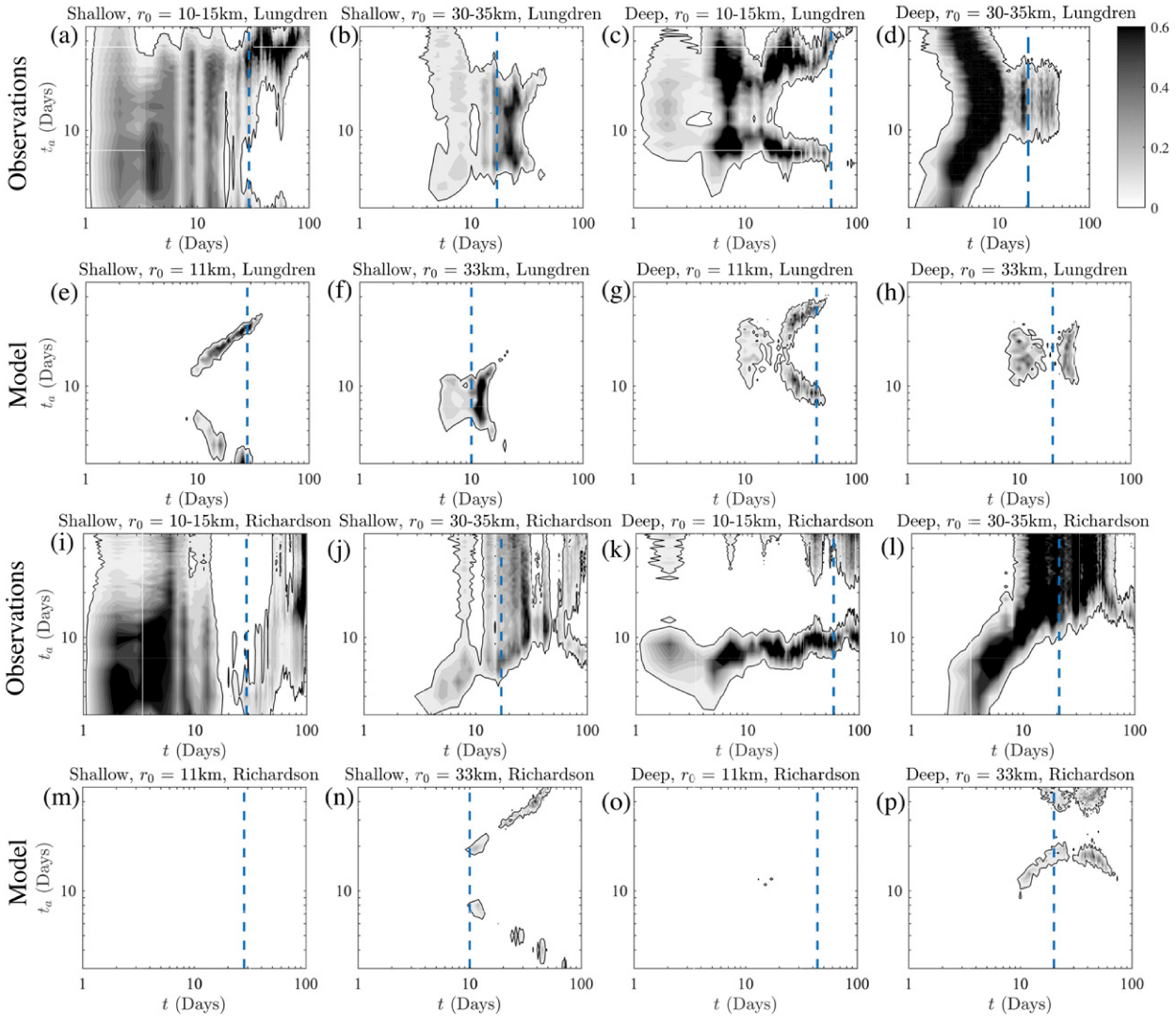

FIG. B3. Kolmogorov–Smirnov test statistic comparing the measured PDFs to the theoretical PDFs, plotted as a function of time and time over which the relative dispersion is fit to estimate the parameters (t_a). A value greater than 0.05, marked by black contour line, suggests that the measured and theoretical PDFs are statistically similar. Rows 1 and 3 [(a)–(d) and (i)–(l)] compare the float PDFs to the nonlocal and Richardson dispersion, while rows 2 and 4 [(e)–(h) and (m)–(p)] compare the particle PDFs to the nonlocal and Richardson dispersion. The dashed blue vertical line corresponds to the time when the mean pair separation (r^*) reaches 100 km. The depth and initial separation (r_0) are indicated in the panel titles.

r_0 = 11 km (Figs. B3m,o), while a match over a very short time period is seen for r_0 = 33 km (Figs. B3n,p). Notably none of the particle sets matched either of the theoretical PDFs over the first 5–10 days; this might be because the particles experienced ballistic dispersion during this time (shown next). Overall, these results suggest that the numerical model shows nonlocal dispersion as expected.

The relative dispersion from the particles for the first 3–4 days also showed a slower growth rate than exponential (Figs. 5b,e), which is likely the result of dependence on initial conditions and ballistic growth. Trajectory pairs need to lose memory of their initial conditions for the canonical scaling relationships to be expressed (Babiano et al. 1990; Nicolleau and Yu 2004; Bourgoin et al. 2006; Foussard et al. 2017). We quantify the rate of loss of memory of the initial conditions using a memory index, $M(t|r_0) = \langle \mathbf{r} \cdot \mathbf{r}_0 \rangle_{r_0} / r_0 \overline{r^2}^{1/2}$, which is a measure of correlation between the pair orientation relative to its initial orientation (Foussard et al. 2017). Both floats and particles lose memory of their initial orientation as time progresses (Fig. B4a). The memory index $M(t)$ for the floats is almost insensitive to the depth but depends strongly on r_0, while $M(t)$ for the particles varies more strongly with depth and is relatively insensitive to r_0.

During the initial phase, when pairs have not lost memory of their initial conditions, the pairs disperse ballistically [$\overline{r^2}(t) = r_0^2(1 + C_1 t^2)$]. Since different choices of depth and r_0 lead to

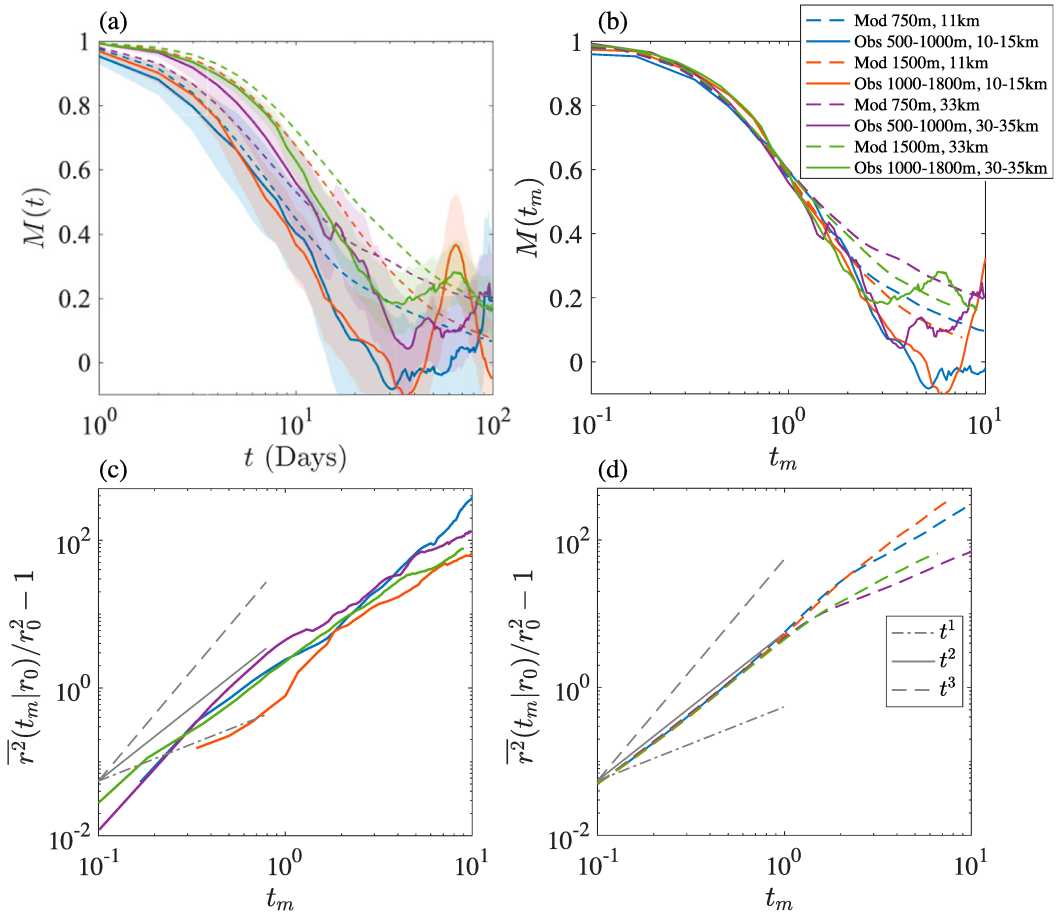

FIG. B4. (a) The memory index, quantifying how quickly the dependence on initial condition is lost for all different choices of depth and r_0. The legend for all the figures in shown in (b). (b) The memory index plotted as a function of rescaled time $t_m = t/\tau_m$, where τ_m is the time it takes for $M(t)$ to reach a value of 0.6. (c) Float and (d) particle relative dispersion plotted in compensated form as a function of rescaled time t_m, to identify if a ballistic regime is observed. In (c) and (d) power laws have been plotted for reference as labeled in the legend in (d).

different evolution of $M(t)$, we define a time scale τ_m as the time it takes for $M(t)$ to reach a value of 0.6, and rescale time using this time scale, $t_m = t/\tau_m$. The factor of 0.6 was chosen because it caused all the different rescaled relative dispersion curves $[\overline{r^2}(t_m|r_0)/r_0^2 - 1]$ for the particles to collapse together during this initial phase (Fig. B4d), and also caused $M(t_m)$ to approximately collapse (Fig. B4b). The particles show a perfect ballistic growth up to approximately $\sim 0.5 t_m$, after which the different curves diverge. The range of this ballistic growth is observed approximately to length scales of $r^* \approx 2$–$3r_0$, which are within the numerical model's viscous range. Foussard et al. (2017) also observed a similar ballistic range in a family of two dimensional numerical models, and noted that the departure from the ballistic regime seemed to occur around the time that the mean separation became comparable to the smallest length scales corresponding to the start of the inertial ranges. The rescaled relative dispersion curves from the floats did not show such a clear range of quadratic growth, and were relatively noisy (Fig. B4c), which is probably a result of high-frequency variability resulting in a very rapid loss of memory of initial conditions that is not properly quantified by $M(t)$.

APPENDIX C

Relative Diffusivity and Waves

Here we show that waves, which can be a dominant part of energy spectrum or the second-order structure function at the submesoscales, may not impact the relative diffusivity. As κ is related to the relative velocity autocorrelation, it can be expressed in terms of the wavenumber–frequency energy spectrum (Bennett 1984; Babiano et al. 1990), as

$$\kappa(r,t) = 2\int_0^\infty\int_0^\infty \left\{ E_{ll}(k,\omega)[1 - J_0(kr)]\int_0^t R(k,\omega,\tau)\, d\tau \right\} d\omega\, dk. \tag{C1}$$

This equation is similar to Eq. (2) for the longitudinal second-order structure function, except that it is weighted

by the integral of the normalized wavenumber–frequency Lagrangian energy spectrum $R(k, \omega, \tau)$. The energy spectrum $R(k, \omega, \tau)$ is the Lagrangian autocorrelation for flows of wavenumber k and frequency ω, defined as $R(k, \omega, \tau) = U_{ll}(k, \omega, \tau)/U_{ll}(k, \omega, 0)$, where

$$U_{ll}(k,\omega,\tau) = \frac{1}{(2\pi)^3}\iiint \langle u_l(\mathbf{x}+\mathbf{r}, t+T, t) \times u_l(\mathbf{x}, t, t-\tau)\rangle \exp(i\mathbf{k}\cdot\mathbf{r} + \omega T)\, d^2\mathbf{r}\, dT\,, \qquad \text{(C2)}$$

and $U_{ll}(k, \omega, 0) = (2\pi k)^{-1} E_{ll}(k, \omega)$. The term $u_l(x, t, t - \tau)$ is the longitudinal velocity at time $(t - \tau)$ of a trajectory $\mathbf{r}$ that passes through $\mathbf{x}$ at time t, while $u_l(\mathbf{x} + \mathbf{r}, t + T, t)$ is the longitudinal velocity at time $t + T$ at a location $\mathbf{x} + \mathbf{r}$. The purpose of having two time lags: an Eulerian time (T) and a Lagrangian time (τ), in contrast to only a Lagrangian time as in Bennett (1984), is to be able to do a spectral decomposition in frequency. The dependence on $\mathbf{x}$ and t on is dropped assuming homogeneity in space and stationarity in time of the underlying Eulerian flow field.

At small times the $R(k, \omega, \tau)$ is 1, and $\kappa(r, t) \approx tS2_{ll}(r)$; implying that the relative diffusivity and second-order structure function follow the same scaling (Babiano et al. 1990). If time is longer than the integral time scales $[t \gg T_I(\kappa, \omega)]$ for all wavenumbers and frequencies but smaller than the uncorrelated limit, then the relative diffusivity follows,

$$\kappa(r) = 2\int_0^\infty\int_0^\infty \{E_{ll}(k,\omega) T_I(k,\omega)[1 - J_0(kr)]\}\, d\omega\, dk\,. \qquad \text{(C3)}$$

Here $T_I(k, \omega) = \int_0^\infty R(k, \omega, \tau)\, d\tau$ acts as a filter in Eq. (C3), and modulates the extent to which the $E_{ll}(k, \omega)$ at each wavenumber and frequency impacts the stirring. The integral time scale that is usually estimated from the single-particle velocity autocorrelation (LaCasce 2008; Balwada et al. 2016b) is equivalent to the integral of $T_I(k, \omega)$ over all wavenumber and frequency. The estimate of relative diffusivity in Eq. (C3) is the estimate that we are interested in, since we care about the integrated impacts of stirring.

Since linear waves do not contribute significantly to stirring (Holmes-Cerfon et al. 2011; Bühler et al. 2013), the wavenumbers and frequencies composed primarily of waves will have $T_I \approx 0$ and the kinetic energy of these scales will not contribute to the relative diffusivity estimate in Eq. (7). Balwada et al. (2018) showed that a conceptually similar result is also true for the time-mean vertical tracer flux, where the wavenumber–frequency energy spectrum of the vertical velocity has a dominant peak at the superinertial frequencies, as a result of linear waves, but the corresponding cross-spectrum of the vertical tracer flux has no contribution from these scales. Scaling based estimates of relative diffusivity (discussed toward the end of section 4a), which stem from 2D turbulence theory, assume the flow is not composed of any linear waves, and thus all of the kinetic energy spectrum contributes to the relative diffusivity.

REFERENCES

Abernathey, R., and D. Ferreira, 2015: Southern ocean isopycnal mixing and ventilation changes driven by winds. *Geophys. Res. Lett.*, **42**, 10–357, https://doi.org/10.1002/2015GL066238.

Artale, V., G. Boffetta, A. Celani, M. Cencini, and A. Vulpiani, 1997: Dispersion of passive tracers in closed basins: Beyond the diffusion coefficient. *Phys. Fluids*, **9**, 3162–3171, https://doi.org/10.1063/1.869433.

Babiano, A., C. Basdevant, and R. Sadourny, 1985: Structure functions and dispersion laws in two-dimensional turbulence. *J. Atmos. Sci.*, **42**, 941–949, https://doi.org/10.1175/1520-0469(1985)042<0941:SFADLI>2.0.CO;2.

——, ——, P. Le Roy, and R. Sadourny, 1990: Relative dispersion in two-dimensional turbulence. *J. Fluid Mech.*, **214**, 535–557, https://doi.org/10.1017/S0022112090000258.

Bachman, S. D., B. Fox-Kemper, and B. Pearson, 2017: A scale-aware subgrid model for quasi-geostrophic turbulence. *J. Geophys. Res. Oceans*, **122**, 1529–1554, https://doi.org/10.1002/2016JC012265.

Balwada, D., J. H. LaCasce, and K. G. Speer, 2016a: Scale dependent distribution of kinetic energy from surface drifters in the Gulf of Mexico. *Geophys. Res. Lett.*, **43**, 10 856–10 863, https://doi.org/10.1002/2016GL069405.

——, K. G. Speer, J. H. LaCasce, W. B. Owens, J. Marshall, and R. Ferrari, 2016b: Circulation and stirring in the southeast Pacific Oean and the scotia sea sectors of the Antarctic Circumpolar Current. *J. Phys. Oceanogr.*, **46**, 2005–2027, https://doi.org/10.1175/JPO-D-15-0207.1.

——, K. S. Smith, and R. Abernathey, 2018: Submesoscale vertical velocities enhance tracer subduction in an idealized antarctic circumpolar current. *Geophys. Res. Lett.*, **45**, 9790–9802, https://doi.org/10.1029/2018GL079244.

Bennett, A., 1984: Relative dispersion: Local and nonlocal dynamics. *J. Atmos. Sci.*, **41**, 1881–1886, https://doi.org/10.1175/1520-0469(1984)041<1881:RDLAND>2.0.CO;2.

——, 2006: *Lagrangian Fluid Dynamics*. Cambridge University Press, 286 pp.

Berger, V. W., and Y. Zhou, 2014: Kolmogorov–Smirnov test: Overview. *Wiley StatsRef: Statistics Reference Online*, N. Balakrishnan et al., Eds., Wiley, https://doi.org/10.1002/9781118445112.stat06558.

Beron-Vera, F. J., and J. H. LaCasce, 2016: Statistics of simulated and observed pair separations in the Gulf of Mexico. *J. Phys. Oceanogr.*, **46**, 2183–2199, https://doi.org/10.1175/JPO-D-15-0127.1.

Berrisford, P., D. P. Dee, M. Fielding, M. Fuentes, P. W. Kallberg, S. Kobayashi, and S. Uppala, 2009: The ERA-Interim archive. ERA Rep. Series 1, 16 pp., https://www.ecmwf.int/node/8173.

Boland, E. J. D., E. Shuckburgh, P. H. Haynes, J. R. Ledwell, M.-J. Messias, and A. J. Watson, 2015: Estimating a submesoscale diffusivity using a roughness measure applied to a tracer release experiment in the southern ocean. *J. Phys. Oceanogr.*, **45**, 1610–1631, https://doi.org/10.1175/JPO-D-14-0047.1.

Bourgoin, M., N. T. Ouellette, H. Xu, J. Berg, and E. Bodenschatz, 2006: The role of pair dispersion in turbulent flow. *Science*, **311**, 835–838, https://doi.org/10.1126/science.1121726.

Bracco, A., J. Choi, K. Joshi, H. Luo, and J. C. McWilliams, 2016: Submesoscale currents in the northern Gulf of Mexico: Deep phenomena and dispersion over the continental slope. *Ocean Modell.*, **101**, 43–58, https://doi.org/10.1016/j.ocemod.2016.03.002.

Bühler, O., N. Grisouard, and M. Holmes-Cerfon, 2013: Strong particle dispersion by weakly dissipative random internal waves. *J. Fluid Mech.*, **719**, 719, https://doi.org/10.1017/jfm.2013.71.

Chelton, D. B., R. A. DeSzoeke, M. G. Schlax, K. El Naggar, and N. Siwertz, 1998: Geographical variability of the first baroclinic Rossby radius of deformation. *J. Phys. Oceanogr.*, **28**,

433–460, https://doi.org/10.1175/1520-0485(1998)028<0433:GVOTFB>2.0.CO;2.

Corrado, R., G. Lacorata, L. Palatella, R. Santoleri, and E. Zambianchi, 2017: General characteristics of relative dispersion in the ocean. *Sci. Rep.*, **7**, 46291, https://doi.org/10.1038/srep46291.

Cushman-Roisin, B., 2008: Beyond eddy diffusivity: An alternative model for turbulent dispersion. *Environ. Fluid Mech.*, **8**, 543–549, https://doi.org/10.1007/s10652-008-9082-7.

Dewar, W. K., 1980: The effect of internal waves on neutrally buoyant floats and other near-Lagrangian tracers. Ph.D. thesis, Massachusetts Institute of Technology, 78 pp.

Essink, S., V. Hormann, L. R. Centurioni, and A. Mahadevan, 2019: Can we detect submesoscale motions in drifter pair dispersion? *J. Phys. Oceanogr.*, **49**, 2237–2254, https://doi.org/10.1175/JPO-D-18-0181.1.

Forget, G., 2010: Mapping ocean observations in a dynamical framework: A 2004–06 ocean atlas. *J. Phys. Oceanogr.*, **40**, 1201–1221, https://doi.org/10.1175/2009JPO4043.1.

Foussard, A., S. Berti, X. Perrot, and G. Lapeyre, 2017: Relative dispersion in generalized two-dimensional turbulence. *J. Fluid Mech.*, **821**, 358–383, https://doi.org/10.1017/jfm.2017.253.

Fox-Kemper, B., R. Lumpkin, and F. Bryan, 2013: Lateral transport in the ocean interior. *Ocean Circulation and Climate: A 21st Century Perspective*, G. Siedler et al., Eds., International Geophysics Series, Vol. **103**, Academic Press, 185–209, https://doi.org/10.1016/B978-0-12-391851-2.00008-8.

——, and Coauthors, 2019: Challenges and prospects in ocean circulation models. *Front. Mar. Sci.*, **6**, 65, https://doi.org/10.3389/fmars.2019.00065.

Garrett, C., 1983: On the initial streakness of a dispersing tracer in two- and three-dimensional turbulence. *Dyn. Atmos. Oceans*, **7**, 265–277, https://doi.org/10.1016/0377-0265(83)90008-8.

——, 2006: Turbulent dispersion in the ocean. *Prog. Oceanogr.*, **70**, 113–125, https://doi.org/10.1016/j.pocean.2005.07.005.

Gnanadesikan, A., M.-A. Pradal, and R. Abernathey, 2015: Isopycnal mixing by mesoscale eddies significantly impacts oceanic anthropogenic carbon uptake. *Geophys. Res. Lett.*, **42**, 4249–4255, https://doi.org/10.1002/2015GL064100.

Graff, L., S. Guttu, and J. LaCasce, 2015: Relative dispersion in the atmosphere from reanalysis winds. *J. Atmos. Sci.*, **72**, 2769–2785, https://doi.org/10.1175/JAS-D-14-0225.1.

Haza, A. C., T. M. Özgökmen, A. Griffa, A. C. Poje, and M.-P. Lelong, 2014: How does drifter position uncertainty affect ocean dispersion estimates? *J. Atmos. Oceanic Technol.*, **31**, 2809–2828, https://doi.org/10.1175/JTECH-D-14-00107.1.

Holmes-Cerfon, M., O. Bühler, and R. Ferrari, 2011: Particle dispersion by random waves in the rotating Boussinesq system. *J. Fluid Mech.*, **670**, 150–175, https://doi.org/10.1017/S0022112010005240.

Jones, C., and R. P. Abernathey, 2019: Isopycnal mixing controls deep ocean ventilation. *Geophys. Res. Lett.*, **46**, 13 144–13 151, https://doi.org/10.1029/2019GL085208.

Kämpf, J., and D. Cox, 2016: Towards improved numerical schemes of turbulent lateral dispersion. *Ocean Modell.*, **106**, 1–11, https://doi.org/10.1016/j.ocemod.2016.08.003.

Kilbourne, B. F., and J. B. Girton, 2015: Quantifying high-frequency wind energy flux into near-inertial motions in the southeast pacific. *J. Phys. Oceanogr.*, **45**, 369–386, https://doi.org/10.1175/JPO-D-14-0076.1.

Koszalka, I., J. LaCasce, and K. Orvik, 2009: Relative dispersion in the Nordic Seas. *J. Mar. Res.*, **67**, 411–433, https://doi.org/10.1357/002224009790741102.

——, ——, M. Andersson, K. Orvik, and C. Mauritzen, 2011: Surface circulation in the Nordic Seas from clustered drifters. *Deep-Sea Res. I*, **58**, 468–485, https://doi.org/10.1016/j.dsr.2011.01.007.

LaCasce, J., 2008: Statistics from Lagrangian observations. *Prog. Oceanogr.*, **77**, 1–29, https://doi.org/10.1016/j.pocean.2008.02.002.

——, 2010: Relative displacement probability distribution functions from balloons and drifters. *J. Mar. Res.*, **68**, 433–457, https://doi.org/10.1357/002224010794657155.

——, 2016: Estimating eulerian energy spectra from drifters. *Fluids*, **1**, 33, https://doi.org/10.3390/fluids1040033.

——, and A. Bower, 2000: Relative dispersion in the subsurface North Atlantic. *J. Mar. Res.*, **58**, 863–894, https://doi.org/10.1357/002224000763485737.

——, and C. Ohlmann, 2003: Relative dispersion at the surface of the Gulf of Mexico. *J. Mar. Res.*, **61**, 285–312, https://doi.org/10.1357/002224003322201205.

——, R. Ferrari, J. Marshall, R. Tulloch, D. Balwada, and K. Speer, 2014: Float-derived isopycnal diffusivities in the dimes experiment. *J. Phys. Oceanogr.*, **44**, 764–780, https://doi.org/10.1175/JPO-D-13-0175.1.

Ledwell, J. R., A. J. Watson, and C. S. Law, 1998: Mixing of a tracer in the pycnocline. *J. Geophys. Res.*, **103**, 21 499–21 529, https://doi.org/10.1029/98JC01738.

——, E. Montgomery, K. Polzin, L. S. Laurent, R. Schmitt, and J. Toole, 2000: Evidence for enhanced mixing over rough topography in the abyssal ocean. *Nature*, **403**, 179–182, https://doi.org/10.1038/35003164.

——, L. C. St. Laurent, J. B. Girton, and J. M. Toole, 2011: Diapycnal mixing in the Antarctic Circumpolar Current. *J. Phys. Oceanogr.*, **41**, 241–246, https://doi.org/10.1175/2010JPO4557.1.

——, R. He, Z. Xue, S. F. DiMarco, L. J. Spencer, and P. Chapman, 2016: Dispersion of a tracer in the deep gulf of Mexico. *J. Geophys. Res. Oceans*, **121**, 1110–1132, https://doi.org/10.1002/2015JC011405.

Lilly, J., 2019: jlab: A data analysis package for matlab, v. 1.6.6. http://www.jmlilly.net/jmlsoft.html.

Lumpkin, R., and S. Elipot, 2010: Surface drifter pair spreading in the north atlantic. *J. Geophys. Res.*, **115**, C12017, https://doi.org/10.1029/2010JC006338.

Marshall, J., and K. Speer, 2012: Closure of the meridional overturning circulation through southern ocean upwelling. *Nat. Geosci.*, **5**, 171–180, https://doi.org/10.1038/ngeo1391.

Morel, P., and M. Larceveque, 1974: Relative dispersion of constant-level balloons in the 200-mb general circulation. *J. Atmos. Sci.*, **31**, 2189–2196, https://doi.org/10.1175/1520-0469(1974)031<2189:RDOCBI>2.0.CO;2.

Nicolleau, F., and G. Yu, 2004: Two-particle diffusion and locality assumption. *Phys. Fluids*, **16**, 2309–2321, https://doi.org/10.1063/1.1736673.

Okubo, A., 1971: Oceanic diffusion diagrams. *Deep-Sea Res. Oceanogr. Abst.*, **18**, 789–802, https://doi.org/10.1016/0011-7471(71)90046-5.

Ollitrault, M., C. Gabillet, and A. C. De Verdiere, 2005: Open ocean regimes of relative dispersion. *J. Fluid Mech.*, **533**, 381–407, https://doi.org/10.1017/S0022112005004556.

Orsi, A. H., T. Whitworth, and W. D. Nowlin, 1995: On the meridional extent and fronts of the Antarctic Circumpolar Current. *Deep-Sea Res. I*, **42**, 641–673, https://doi.org/10.1016/0967-0637(95)00021-W.

Poje, A. C., and Coauthors, 2014: Submesoscale dispersion in the vicinity of the deepwater horizon spill. *Proc. Natl. Acad. Sci. USA*, **111**, 12 693–12 698, https://doi.org/10.1073/pnas.1402452111.

Polzin, K., and R. Ferrari, 2004: Isopycnal dispersion in NATRE. *J. Phys. Oceanogr.*, **34**, 247–257, https://doi.org/10.1175/1520-0485(2004)034<0247:IDIN>2.0.CO;2.

Richardson, L. F., 1926: Atmospheric diffusion shown on a distance-neighbour graph. *Proc. Roy. Soc. London*, **110A**, 709–737, https://doi.org/10.1098/rspa.1926.0043.

Roach, C. J., D. Balwada, and K. Speer, 2016: Horizontal mixing in the southern ocean from Argo float trajectories. *J. Geophys. Res. Oceans*, **121**, 5570–5586, https://doi.org/10.1002/2015JC011440.

——, ——, and ——, 2018: Global observations of horizontal mixing from Argo float and surface drifter trajectories. *J. Geophys. Res. Oceans*, **123**, 4560–4575, https://doi.org/10.1029/2018JC013750.

Rossby, T., D. Dorson, and J. Fontaine, 1986: The RAFOS system. *J. Atmos. Oceanic Technol.*, **3**, 672–679, https://doi.org/10.1175/1520-0426(1986)003<0672:TRS>2.0.CO;2.

Sansón, L. Z., 2015: Surface dispersion in the Gulf of California. *Prog. Oceanogr.*, **137**, 24–37, https://doi.org/10.1016/j.pocean.2015.04.008.

Siegelman, L., 2020: Energetic submesoscale dynamics in the ocean interior. *J. Phys. Oceanogr.*, **50**, 727–749, https://doi.org/10.1175/JPO-D-19-0253.1.

Sinha, A., D. Balwada, N. Tarshish, and R. Abernathey, 2019: Modulation of lateral transport by submesoscale flows and inertia-gravity waves. *J. Adv. Model. Earth Syst.*, **11**, 1039–1065, https://doi.org/10.1029/2018MS001508.

Srinivasan, K., J. C. McWilliams, M. J. Molemaker, and R. Barkan, 2019: Submesoscale vortical wakes in the lee of topography. *J. Phys. Oceanogr.*, **49**, 1949–1971, https://doi.org/10.1175/JPO-D-18-0042.1.

Sundermeyer, M. A., and J. F. Price, 1998: Lateral mixing and the North Atlantic Tracer Release Experiment: Observations and numerical simulations of Lagrangian particles and a passive tracer. *J. Geophys. Res.*, **103**, 21 481–21 497, https://doi.org/10.1029/98JC01999.

——, J. R. Ledwell, N. S. Oakey, and B. J. Greenan, 2005: Stirring by small-scale vortices caused by patchy mixing. *J. Phys. Oceanogr.*, **35**, 1245–1262, https://doi.org/10.1175/JPO2713.1.

Swift, D. D., and S. C. Riser, 1994: RAFOS floats: Defining and targeting surfaces of neutral buoyancy. *J. Atmos. Oceanic Technol.*, **11**, 1079–1092, https://doi.org/10.1175/1520-0426(1994)011<1079:RFDATS>2.0.CO;2.

Taylor, G. I., 1922: Diffusion by continuous movements. *Proc. London Math. Soc.*, **2**, 196–212, https://doi.org/10.1112/plms/s2-20.1.196.

Thomas, J., and R. Yamada, 2019: Geophysical turbulence dominated by inertia–gravity waves. *J. Fluid Mech.*, **875**, 71–100, https://doi.org/10.1017/jfm.2019.465.

Thomson, R. E., and W. J. Emery, 2014: *Data Analysis Methods in Physical Oceanography*. Elsevier, 654 pp.

Tulloch, R., and Coauthors, 2014: Direct estimate of lateral eddy diffusivity upstream of Drake Passage. *J. Phys. Oceanogr.*, **44**, 2593–2616, https://doi.org/10.1175/JPO-D-13-0120.1.

Uchida, T., D. Balwada, R. Abernathey, G. McKinley, S. Smith, and M. Lévy, 2019: The contribution of submesoscale over mesoscale eddy iron transport in the open Southern Ocean. *J. Adv. Model. Earth Syst.*, **11**, 3934–3958, https://doi.org/10.1029/2019MS001805.

——, ——, R. P. Abernathey, G. A. McKinley, S. K. Smith, and M. Lévy, 2020: Vertical eddy iron fluxes support primary production in the open Southern Ocean. *Nat. Commun.*, **11**, 1–8, https://doi.org/10.1038/s41467-020-14955-0.

van Sebille, E., S. Waterman, A. Barthel, R. Lumpkin, S. R. Keating, C. Fogwill, and C. Turney, 2015: Pairwise surface drifter separation in the western Pacific sector of the Southern Ocean. *J. Geophys. Res. Oceans*, **120**, 6769–6781, https://doi.org/10.1002/2015JC010972.

Vic, C., J. Gula, G. Roullet, and F. Pradillon, 2018: Dispersion of deep-sea hydrothermal vent effluents and larvae by submesoscale and tidal currents. *Deep-Sea Res. I*, **133**, 1–18, https://doi.org/10.1016/j.dsr.2018.01.001.

Waterman, S., A. C. Naveira Garabato, and K. L. Polzin, 2013: Internal waves and turbulence in the Antarctic Circumpolar Current. *J. Phys. Oceanogr.*, **43**, 259–282, https://doi.org/10.1175/JPO-D-11-0194.1.

Watson, A. J., J. R. Ledwell, M.-J. Messias, B. A. King, N. Mackay, M. P. Meredith, B. Mills, and A. C. N. Garabato, 2013: Rapid cross-density ocean mixing at mid-depths in the Drake Passage measured by tracer release. *Nature*, **501**, 408–411, https://doi.org/10.1038/nature12432.

Young, W., P. Rhines, and C. Garrett, 1982: Shear-flow dispersion, internal waves and horizontal mixing in the ocean. *J. Phys. Oceanogr.*, **12**, 515–527, https://doi.org/10.1175/1520-0485(1982)012<0515:SFDIWA>2.0.CO;2.

Yu, X., A. C. Naveira Garabato, A. P. Martin, C. E. Buckingham, L. Brannigan, and Z. Su, 2019: An annual cycle of submesoscale vertical flow and restratification in the upper ocean. *J. Phys. Oceanogr.*, **49**, 1439–1461, https://doi.org/10.1175/JPO-D-18-0253.1.

Zanna, L., 2019: Ocean transport and eddy energy. Tech. Doc., 23 pp., https://doi.org/10.6084/m9.figshare.10105922.v1.

Zhurbas, V., and I. S. Oh, 2003: Lateral diffusivity and Lagrangian scales in the pacific ocean as derived from drifter data. *J. Geophys. Res.*, **108**, 3141, https://doi.org/10.1029/2002JC001596.

Zika, J. D., J.-B. Sallée, A. J. S. Meijers, A. C. Naveira-Garabato, A. J. Watson, M.-J. Messias, and B. A. King, 2020: Tracking the spread of a passive tracer through Southern Ocean water masses. *Ocean Sci.*, **16**, 323–336, https://doi.org/10.5194/os-16-323-2020.